Revision 2 **Word count: 7704**

Multiple magmatic processes revealed by distinct clinopyroxene populations in the magma plumbing system: a case study from a Miocene volcano in West Qinling, Central China

Guo-Kun Zhang[1,2], Xiao-Wei Li[1,2,3*], Ji-Feng Xu[1], Fang-Yue Wang[4], Bader Thomas[5], Guang-Yue Cao[6], Feng Huang[1], Xuan-Xue Mo[1], Wei Shan[3], Da-Peng Li[3], Guo-Chen Dong[1]

[1]State Key Laboratory of Geological Processes and Mineral Resources, School of Earth Sciences and Resources, China University of Geosciences, Beijing 100083, China

[2]Research Center of Genetic Mineralogy, China University of Geosciences, Beijing 100083, China

[3]Shandong Institute and Laboratory of Geological Sciences, and Key Laboratory of Gold Mineralization Processes and Resource Utilization, Jinan 250013, China

[4]Ore Deposit and Exploration Centre, Hefei University of Technology, and School of Resources and Environmental Engineering, Hefei University of Technology, Hefei 230009, China

[5]Key Laboratory of Orogenic Belts and Crustal Evolution, MOE, School of Earth and Space Science, Peking University, Beijing 100085, China

[6]Beijing SHRIMP Center, Institute of Geology, Chinese Academy of Geological Sciences, Beijing 100037, China

DOI: https://doi.org/10.2138/am-2022-8744. http://www.minsocam.org/

Corresponding author: Xiao-Wei Li E-mail address: xwli@cugb.edu.cn

Abstract

The application of whole rock compositions to trace magma evolution or crystal-melt equilibrium may be called into question when foreign crystals are incorporated into host magmas. To address this challenge, establishing the origins (orthocrysts, antecrysts, xenocrysts, etc.) of minerals with variable textures in magmatic plumbing systems is necessary. In this paper, we describe complex oscillatory zoning patterns of clinopyroxenes (Cpx) from the Miocene Majuangou (MJG) alkali basalts from West Qinling. Our detailed petrographic, mineralogical, and geochemical analyses unravel the origins of various Cpx crystals with distinct textural patterns, thereby providing information about magma storage, recharging and/or mixing, and transportation, as well as the reactions between crystals and melt/fluid. Based on textural patterns, Cpx may be divided into four types with normal (Type–1 Cpx), simple oscillatory (Type–2 Cpx), complex oscillatory (Type–3 Cpx), and grains that lack zoning (Type–4 Cpx, suggested to be orthocrysts). Through the textural characterization of Cpx, the comparison between different types of Cpx, and the relationships between Cpx major compositions from different lithologies, we concluded that Type 1, 2 and 3 Cpx cores are antecrysts or xenocrysts with diverse origins: primitive magma (Type–1 Cpx cores), magma mush (Type–2 Cpx cores), and crustal granulite (Type–3 Cpx cores). The zoning patterns and the compositions of these Cpx crystals indicate at least three batches of magmatic activity, i.e., the Batch-1 low-Mg# magma (Mg#: 47.4–53.3), the Batch-2 primitive magma (Mg#: 57.2–64.5), and the Batch-3 low-Mg# host alkali magma (Mg#: 47.2–54.6). Cpx-melt thermobarometry demonstrates that at least two crustal magma reservoirs existed in the magma plumbing system at depths of 30.1 km and 40.9 km. The antecrystic/xenocrystic Cpx cores were captured by, continued to grow in, and subsequently reacted with ascending K-rich melt/fluid. The spongy textures in Cpx cores/mantles are attributed to this reaction, which may be expressed as: Melt 1 (primitive or evolved) + K-rich melts/fluids + Cpx ($CaMgSi_2O_6$) = K-feldspar ($KAlSi_3O_8$) + Ilmenite ($FeTiO_3$) + Melt 2 (derivative). The products of this reaction (K-feldspar and ilmenite) filled the sieves in the spongy zones of Type 1–3 Cpx. This detailed investigation of compositional and textural features of Cpx antecrysts/xenocrysts suggests that the interactions between various interconnected magma reservoirs are widespread beneath the magmatic plumbing system. Our study emphasizes the importance of the Cpx-melt/fluid reaction in magmatic plumbing system, which can significantly modify the whole-rock compositions and lead to the formation of spongy textures without the need for fractures and cracks in minerals.

Keywords: alkali basalts; zoning texture; spongy texture; crystal-melt/fluid reaction; Cpx antecrysts/xenocrysts

Introduction

Details of pre-eruptive magma storage, transport, and evolution are essential to reconstruct transcrustal magma plumbing systems, to reveal the histories of eruptions, and to monitor potential volcanic activities (Ganne et al. 2018; Ubide et al. 2019a;

Magee et al. 2021; Pontesilli et al. 2021; Ubide et al., 2021). Previous studies have demonstrated that a basaltic magmatic system usually consists of multiple, interconnected, vertically distributed magma storage layers and reservoirs within the upper mantle and the crust, which feed small (ephemeral) magma reservoirs at shallow-crustal levels. The eruptive rocks are final products recording the interaction between different magma chambers or magma mushes (Cashman et al. 2017; Magee et al. 2018; van Gerve et al. 2020; Lucci et al. 2020).

As one of the main components in basaltic rocks, crystals (olivine, pyroxene or plagioclase) with various origins typically record crucial information for multistep magma transport, recharge and storage within the Earth's mantle and crust (Zhang et al. 2007; Ubide et al. 2019a, 2019b, 2021; Masotta et al. 2020). The crystals carried by the volcanic eruptions hold clues of melt compositions and magmatic conditions, thereby providing windows into processes that are physically inaccessible yet control volcanic behavior and the evolution of magmatic systems (Ubide et al. 2021; Edmonds et al. 2019). Specifically, these crystal populations may be classified as orthocrysts, antecrysts, xenocrysts, or peritectic phases (Miller et al. 2007; Jerram and Martin 2008; Bach et al. 2012). Xenocrysts are crystals that originated from disaggregated crustal/mantle xenoliths; orthocrysts crystallized directly from their host magmas; antecrysts did not directly crystallize from the host magmas but are spatially and temporally related to the magmatic plumbing system (Miller et al. 2007). The term phenocryst describes larger crystals that are either orthocrysts or antecrysts in the host.

Recently updated conceptual models of transcrustal magmatic systems (Cashman et al. 2017; Magee et al. 2018; van Gerve et al. 2020) have raised questions of how magmas from various reservoirs are assembled prior to eruption and how antecrysts or xenocrysts interact with host magmas or fluids in the magmatic system at multiple crustal levels. Textural characteristics, chemistry, and style of compositional zoning of crystals are sensitive to magma compositions and conditions during crystallization. In particular, zoning textures within minerals testify complex dynamic processes that result from the interaction between different magmas, such as magma differentiation, mixing/recharging, and the assimilation of pre-existing crust or mantle materials (Streck 2008; Cashman and Blundy 2013; Xing and Wang 2020; Palummo et al. 2021; Cao et al. 2022). Furthermore, spongy textures that are common in minerals from mantle xenoliths and volcanic rocks, may provide crucial information on pre-eruptive processes as well as the nature and evolution of the deep mantle, e.g., magma transport or residence and mantle metasomatism (Shaw et al. 2006; Su et al. 2011; Ma et al. 2015). Hence, determining the origins of textures and compositions of these crystals can provide critical insight to the interaction between distinct magma reservoirs in the magmatic plumbing system, the reaction between crystals and the host melts/fluids, and the magmatic evolution of discrete magma reservoirs at depth (Su et al. 2011; Shaw et al. 2006; Liu et al. 2012).

As an important and ubiquitous liquidus phase in mantle-derived magmas, clinopyroxene may crystallize across a broad range of pressures and water contents (Putirka 2008; Armienti et al. 2013; Cristina et al. 2019; Ubide et al. 2019a). Its chemical compositions are sensitive to pressure, temperature, water content, and magma composition (e.g., Putirka 2008; Ubide et al. 2019a). Combined with the relatively slow elemental diffusion in clinopyroxene (Cpx) in comparison with olivine in alkali basalts (Müller et al. 2013), the favorable physicochemical properties ensure that Cpx crystals can serve as reliable recorders of transcrustal magmatic processes and evidence of crystal recycling with both cognate and non-cognate origins. The incorporation of foreign crystal populations will modify the whole-rock compositions, therefore the textural characteristics and compositional data of Cpx crystals may provide more robust evidence than the whole-rock compositions alone (Luo et al. 2018). Clinopyroxenes are therefore widely used to reconstruct the evolution of magmatic plumbing systems and provide crucial information about the details of crystal-fluid/melt interactions in magmatic plumbing systems (Coote and Shane 2018; Feng and Zhu 2018, 2019; Li et al. 2020).

In this paper, we focus on the Miocene alkali basalts in the Majuangou (MJG) area of West Qinling, Central China. Previous studies have established that the West Qinling orogen has a thickened crust (~52 km, Zhang et al. 2020) and a widespread occurrence of alkali lavas in the Cenozoic (Yu et al. 2009). The large crustal thickness and the extensive alkali magmatic activity allow the potential storage regions spanning a wide range of depths. Thus, these alkali basalts and the crystals they hold may serve as suitable candidates for gaining insight into the pre-eruptive evolution of the transcrustal magmatic system. This study combines the textural characteristics and mineral chemistry of Cpx crystals to identify the sources of various Cpx crystals, to determine the genesis of zoning and spongy textures, and to calculate the crystallization pressures.

We aim to reconstruct a complex magmatic plumbing system, to reveal pre-eruptive processes (magma transport, recharge, and storge), and to decipher the details of the interaction between Cpx antecrysts/xenocrysts and the host melt/fluid.

Geological Setting and Sample Descriptions

West Qinling is located between the Songpan-Garzê terrane and the Qilian orogen and tectonically bounded by the Qinghai Lake-Wushan-Tianshui fault to the north, the Mianlue-A'nyemaqen suture zone to the south, and the Wahongshan-Wenquan and Fengxian-Taibai strike-slip faults/Huicheng Basin to the west and east, respectively (Dong et al. 2011; Li et al. 2015; Fig. 1a&b). Cenozoic volcanoes in West Qinling are sparsely distributed in the Tianshui-Lixian fault basin, and ca. 50 outcrops scattered across an area of ca. 4000 km^2 (Yu et al. 2011; Guo et al. 2014; Su et al. 2010). The Cenozoic volcanoes are predominantly cinder cones, pipes, diatreme-tuff rings, and subvolcanic intrusions with a single outcrop area of generally less than 1 km^2, and several lava flows cover areas of a few square kilometers (Su et al. 2010; Guo et al. 2014). These lavas mainly consist of potassic alkali basalts, kamafugites, and associated carbonatites dated at 23.2–7.1 Ma (Yu et al. 2011). Mantle xenoliths are entrained in these alkali basalt lavas, and they have been extensively studied to ascertain the nature of the sub-continental lithosphere and deep processes occurring within the lithospheric mantle beneath West Qinling (e.g., Su et al. 2012).

The Majuangou alkali basalts investigated in this study were sampled from a cinder cone in the Tanchang county, West Qinling. They contain both lherzolite xenoliths and pyroxenite xenoliths (Fig. 2a&b). Thirteen of the twenty samples are classified as trachybasalt, but the remaining seven samples are basalt based on the Total Alkali Silica (TAS) diagram (Le Bas et al. 1986; Fig. S1&Table S1). Both lithologies have identical mineral assemblages. The analyzed Majuangou basalts exhibit a typical porphyritic texture, given 15–20 vol.% of larger crystals among which euhedral-subhedral Cpx dominates over subordinate anhedral olivine (Fig. 2b). The groundmass with intergranular texture consists of euhedral plagioclase and interstitial Cpx, as well as minor olivine and biotite (Fig. 2c). Porphyritic Cpx are subhedral to euhedral with embayed boundary and are found in both lithologies, which generally exhibit spongy textures. The sieves in the spongy zones are filled with K-feldspar and ilmenite as mineral inclusions (Fig. 2g–i). As a minor phase, biotite mainly occurs as biotite glomerocryst or surrounding Cpx glomerocrysts (Fig. 2j–l).

Analytical Methods

Whole-rock major element analysis was carried out at the Guangzhou Institute of Geochemistry, Chinese Academy of Sciences, using an X-ray fluorescence (XRF) spectrometer. Results are reported relative to the USGS rock standards with an analytical accuracy and precision are better than 5%. More details are shown in the supplementary materials.

Electron-probe micro-analysis and X-ray mapping

The major element spot analyses of Cpx, the identification of mineral inclusions, and major element X-ray mapping were conducted with a JEOL JXA–8230 electron microprobe equipped with an Oxford X-Max 80 mm^2 Energy Dispersive Spectrometer (EDS) detector running Oxford INCA X-ray microanalysis software at the Shandong Key Laboratory of Mineralization Geological Processes and Resource Utilization in Metallic Minerals of the Shandong Geological Science Institute. Point analyses were obtained on carbon-coated polished thin-sections under high-vacuum conditions using an accelerating voltage of 15 kV, an electron beam current of 20 nA, a beam diameter of 5–10 μm, and peak and background counting times of 10 s and 5 s, respectively. The standard materials used for calibration were pure oxides and silicates of the Astimex series [sanidine (K), jadeite (Na, Si), diopside (Mg, Ca), rutile (Ti), rhodonite (Mn), olivine (Fe), almandine garnet (Al), and chromium oxide (Cr)], and the results were corrected using the ZAF method (Z, atomic number; A, absorption; F, fluorescence). Astimex chrome diopside was used as quality monitor standard and for the calculation of accuracy and precision. The data of samples and standard material are provided in Table S2. The accuracy was $<$ 2% for major elements ($>$2 wt. %) and $<$ 10% for minor elements ($<$2 wt. %). The analytical precision was better than 2% for major elements and 15% for minor elements.

Mineral inclusions in the sieves within the spongy textures of Type 1–3 Cpx were identified with the EDS detector at 15 kV accelerating voltage and 4 nA electron beam current; the X-rays acquisition was stopped at >300,000 counts per spot.

X-ray maps of the Cpx antecrysts/xenocrysts were made with an accelerating voltage of 15 kV, a beam current of 200 nA, a dwell time of 10 ms, and a pixel size of 1 μm. Each scan analyzed up to 4 elements, and we included the major elements Si, Mg, Al, Fe, Ca, Ti, K, and Na.

In-situ trace element analysis and LA–ICP–MS mapping of minerals

In-situ trace element analysis and LA–ICP–MS mapping of minerals were conducted at the Ore Deposit and Exploration Centre (ODEC), School of Resources and Environmental Engineering, Hefei University of Technology, using an LA–ICP–MS instrument (Agilent 7900) equipped with a Photon Machines Analyte HE 193 nm ArF excimer laser. Helium was used as the carrier gas to enhance the transport efficiency of the ablated material. Spot analyses used a beam size of 40 μm at 10 Hz, and gas blank measurements of 20 s, preceded by data acquisitions of 60 s. Scan analyses of Cpx antecrysts/xenocrysts were conducted at a scanning speed of 15 μm/s at 20–40 Hz with an energy density of 2 J/cm^2. SRM610 were external standards for data calibration without applying an internal standard. SRM612 and BCR–2g glass reference materials were used as secondary standards to monitor accuracy and precision. Offline data processing was performed with the ICPMSDataCal program (Liu et al. 2008). The compositions of standard materials and samples are reported in Supplementary Table 3. The precision is typically better than 10%. The analytical uncertainties are better than ±5% (2σ).

Several zoned Cpx grains were selected for mapping analysis. Different from single-point analysis, the laser beam moved continuously across the mineral surface and the ablated lines are adjacent to each other in order to obtain the full map. A beam diameter of 20 μm, a repetition rate of 10 Hz, an fluence of 3 J/cm^2, and a translation speed of 20 μm/s were used for all experiments. The trace element maps of Cpx were calibrated against SRM 610 reference material without internal standard materials. All these maps are semi-quantitative. The horizontal resolution for LA–ICP–MS mapping of our samples is about 6 μm (where the translation speed of the laser is multiplied by the total integral time of all the elements, Wang et al. 2017), and the vertical resolution is equivalent to the diameter of the laser beam (20 μm). The analytical precision for all elements was better than 10%. The accuracy was better than 30%. Trace element mapping images of Cpx were compiled and processed using LIMS (an in-house designed mapping reduction software based on Matlab). The average background in the image of an element was subtracted from the element's values, and the raster images were compiled into a 2–D image displaying the combined background/drift corrected intensity (Wang et al. 2017).

Results

We analyzed whole-rock major elements for 20 alkali basalt samples from the Majuangou area (Table S1). The supporting information provides the detailed sample descriptions.

Major elements of Cpx crystals

The alkali basalts from West Qinling universally contain Cpx crystals, which either exhibit zoning and spongy texture, or a clean, unzoned appearance. The whole Cpx crystals show a wide compositional range (Table S2), from augite to diposide (Fig. 3), according to the classification of Morimoto (1988). Some Cpx crystals display various zoning patterns (core-rim zoning or core-mantle-rim zoning), indicative of textural and compositional complexities. The augitic pyroxenes are found in the core/mantle zones with high Mg# values (81.1–86.8, Mg# = 100×Mg/(Mg+Fe^{2+})). In contrast, diposide mostly occurs in the rim parts and has a wider range but lower Mg# values (65.4–81.0). Except for the zoned Cpx crystals, unzoned Cpx crystals are mainly in the groundmass and exhibit subhedral to euhedral shapes.

The Cpx crystals in the Majuangou samples may be divided into four types based on their textural features and compositional variations (Fig. 4):

Type–1 Cpx cores have higher Mg# (82.5–86.8) and lower Al_2O_3 (3.03–4.30 wt. %), TiO_2 (0.65–1.41 wt. %), and CaO (20.36–21.85 wt. %) contents than their rims (Mg#: 76.5–81.0, Al_2O_3: 3.59–4.78 wt. %, TiO_2: 2.20–2.97 wt. %, CaO: 21.43–22.33 wt. %; Fig. 5), showing normal zoning (Fig. 6). There is an abrupt change in compositions from cores to rims (Fig. 6). Moreover, the cores of Type–1 Cpx show spongy textures and contain abundant mineral inclusions that are composed of K-feldspar and ilmenite in the sieves determined by the EDS detector and X-ray maps (Fig. 7a-d), while the rims are intact without mineral inclusions. The cores have rounded boundaries, and are obviously in contact with the intact rims.

Type–2 Cpx exhibit pronounced simple oscillatory zonation with resorbed low-Mg# cores, subsequently enclosed by high-Mg# mantles and low-Mg# clean rims (Fig. 4b). The cores and rims of Type–2 Cpx share similar compositions (Fig. 5), displaying lower Mg# (76.1–80.1) but higher Al_2O_3 (2.95–5.71 wt. %), TiO_2 (1.49–3.55 wt. %) and CaO (21.51–22.24 wt. %) contents than their mantles (Fig. 6). The high-Mg# mantles of Type–2 Cpx also show a spongy texture that is similar to the cores of Type–

1 Cpx (Fig. 2h&4), with widths of 60–300 μm in most cases. The sieves in the spongy mantles are also filled by the mineral assemblage of K-feldspar and ilmenite as evidenced by X-ray maps (Fig. 7e-h) and the EDS analysis.

Type–3 Cpx are composed of low-Mg# (65.4–66.3) inner cores, intermediately low-Mg# outer cores (69.7–74.7), high-Mg# mantles (82.0–84.4) and low-Mg# intact (clean) rims (76.4–78.5, Fig. 4). For the core parts, the inner cores have lower Al_2O_3 (1.60–1.69 wt. %), TiO_2 (0.04–0.10 wt. %), and Cr_2O_3 (0–0.06 wt. %) contents but higher CaO (23.08–23.84 wt. %) abundances than the outer cores with Al_2O_3 (1.64–1.78 wt. %), TiO_2 (0.11–0.30 wt. %), Cr_2O_3 (0.01–0.05 wt. %) and CaO (22.85–23.12 wt. %) contents (Fig. 6). Besides, the inner cores show different compositions from those of Type 1–2 Cpx, which are characterized by very low Mg#, Al_2O_3 and TiO_2 contents (Fig. 5). The outer cores have intermediate compositions between the low-Mg# inner cores and high-Mg# mantles (Fig. 6). The mantles are characterized by a spongy texture (Fig. 7i-k), and have comparable compositions with Type–1 Cpx cores and Type–2 Cpx mantles, with high Mg# values, and Al_2O_3 (3.49–3.78 wt. %), CaO (20.45–20.71 wt. %) and TiO_2 (0.95–0.97 wt. %) contents (Fig. 6). The mineral inclusions in the sieves were identified by the EDS detector rather than the X-ray map due to the small sizes, and consist of K-feldspar and ilmenite, identical to the spongy zones in Type 1–2 Cpx.

The rims of Type 1–3 Cpx have the same major compositions, with the Mg# (76.1–81.0), Al_2O_3 (3.58–5.71 wt. %), CaO (21.60–23.02 wt. %) and TiO_2 (1.61–3.55 wt. %).

Type–4 Cpx are unzoned and subhedral to euhedral. Most of them have small sizes

DOI: https://doi.org/10.2138/am-2022-8744. http://www.minsocam.org/

of 100–300 μm, while few of them measure 400–800 μm. Type–4 Cpx exhibit a narrow range of Mg# values (78.2–80.8), show homogeneous compositions (Fig. 5).

Trace elements of Cpx crystals

Except for the Type–3 Cpx cores, Type–1 Cpx, Type–2 Cpx and the other zones (mantles and rims) of Type–3 Cpx are collectively characterized by the same convex-upward rare earth element (REE) pattern similar to Type–4 Cpx, but their concentrations are different (Fig. 8, Table S3).

The high-Mg# cores of Type–1 Cpx exhibit the same convex-upward rare earth element (REE) pattern in the rims but with higher REE contents (Fig. 8a&b). The cores and rims of Type–2 Cpx have identical trace element compositions, exhibiting higher REE contents than their high-Mg# mantles (Fig. 8c&d). The cores of Type–3 Cpx (inner cores and outer cores) have discontinuous and flat REE patterns, unlike other types of Cpx antecrysts/xenocrysts and Cpx orthocrysts (Fig. 8e&f). The high-Mg# mantles of Type–3 Cpx have the same trace element compositions as the other high-Mg# parts in Type 1–2 Cpx (Fig. 8). The Type–4 Cpx (Cpx orthocrysts) exhibit a uniform middle rare earth elements (MREEs) convex-upward distribution pattern with REE contents similar to the rims of Type 1–3 Cpx (Fig. 8).

The rims of Type 1–3 Cpx have a uniform REE pattern, with higher REE contents than the high-Mg# parts (Fig. 8). According to the trace element maps (Fig. S2), the sieves (spongy space) in the spongy zones of Type–1 and Type–3 Cpx are characterized by enrichments in K, Ti, Al, Na, and P, as well as Rb, Sr, and Ba. Rims of Type–1 and Type–3 Cpx do not show such enrichments (Fig. S2). The LA–ICP–MS mapping was not performed for Type–2 Cpx, because fractures frequently occur in Type–2 Cpx, which may cause abnormal element values.

Overall, the compositional trends of Cpx in the Majuangou alkali basalts are the accordance of higher Mg# with lower ∑REE and the opposite.

Discussion

Decoding the origin of the Cpx crystals and the genesis of the zoning texture

In Type 1–3 Cpx, there is a sharp geochemical composition change between the xenomorphic cores and the subhedral-euhedral rims/mantles (Fig. 6). They show various zoning patterns (e.g., normal zoning, simple oscillatory zoning, and complex oscillatory zoning), suggesting significant physicochemical changes of the growth conditions that likely resulted from open-system processes, such as magma recharge or mixing (Streck 2008; Ginibre et al. 2007). In contrast, Type–4 Cpx are unzoned and with small sizes (Fig. 2c), mainly fill the groundmass. Type–4 Cpx are considered to be orthocrysts due to their homogeneous and comparable compositions to the rims of Type 1–3 Cpx (Fig. 5).

In Type–1 Cpx, the mineral composition changes significantly from the core to the rim, indicating contrasting magmatic environments during crystallization (Fig. 6). The compositions of Type–1 Cpx cores are quite different from those of Type–4 Cpx (Fig. 5), and may represent foreign crystals from outside the host magma system, e.g., mantle peridotite, lower crust, or crystallized from previous batch of magma. Compared with Cpx from other sources in West Qinling, the Type–1 Cpx cores have a lower Mg# than

Cpx from mantle peridotite xenoliths in Cenozoic kamafugites (Fig. 9), and they also differ from Cpx from high-pressure granulite (Yang et al. 2018). Thus, Type–1 Cpx cores are neither xenocrysts with mantle or crust origins nor orthocrysts that crystallized from host magmas. Furthermore, Type–1 Cpx cores have lower ∑REE contents but the same REE distribution patterns as the Type–4 Cpx in our samples (Fig. 8), indicating that the Type–1 Cpx cores likely crystallized from an early batch of primitive alkali magma, which is cognate with the host magma of the Type–4 Cpx. Type–1 Cpx show normal zoning, indicating that the high-Mg# cores, as antecrysts, entered more evolved magma, where the low-Mg# rims grew.

The cores of Type–2 Cpx are resorbed and have similar compositions as the rims and Type–4 Cpx, but lower Mg# values than their mantles (Fig. 5&10). This suggests that the Type–2 Cpx cores probably crystallized from an early evolved magma batch that has a similar composition, and is cognate with the host magma where the rims crystallized. Studies on Stromboli volcano have suggested that large Cpx crystals with sizes comparable to Type–2 Cpx (2–4 mm) and resorbed characteristics were derived from the crystal mush zone and recycled by later mafic magmas (Francalanci et al. 2014; Petrone et al. 2018; Ubide et al. 2019b). Such a crystal mush zone may be recharged by multiple batches of magmas, permitting the formation of large crystals (Ubide et al., 2019b). Likewise, the homogeneous compositions and large sizes of Type–2 Cpx cores also imply a stable growth environment and a reservoir supplied continuous recharging, both of which can be provided by magma mush, making it an ideal source for Type-2 Cpx cores. The resorbed characteristics of Type–2 Cpx cores may be formed by the dissolution of antecedent crystals caused by the subsequent magmas (e.g., Ubide et al. 2019b). It is therefore likely that the low-Mg# Type–2 Cpx cores were antecrysts crystallized from an early evolved alkali magma batch, and they could be the fragments of previous magma mush.

Type–2 Cpx show typical oscillatory zoning patterns (Fig 2h&6), indicating variations of the physicochemical conditions in the open magmatic plumbing system. The widths of oscillatory bands in Type–2 Cpx lie typically above 60 μm and can exceed 300 μm in some cases (Fig. 2h). Such broad oscillatory bands and significant compositional differences observed between the core and mantle zones (Fig. 6b) cannot be explained by the chemical diffusion at crystal-melt interface or undercooling of magma (Shore and Fowler 1996; Milman-Barris et al. 2008). They may therefore most likely be attributed to the physicochemical variations of external magma due to the recharge of more primitive alkali magmas (Shore and Fowler 1996; Giacomoni et al. 2016). Additionally, the jagged, rounded boundaries of the Type–2 Cpx cores more likely resulted from the dissolution caused by the replenishment of more primitive alkali magmas (Ginibre et al. 2002). Therefore, it is more reasonable to explain the origin of the oscillatory zoning with primitive magma recharge events. The Cr-Mg enrichment of Type–2 Cpx mantles formed by a hot, mafic magma replenishment (Ubide and Kamber 2018). The similarity of the REE patterns in high-Mg# mantles and low-Mg# rims suggests that the replenished hot, primitive magmas are likely cognate with the host magmas.

The Type–3 Cpx inner cores feature the lowest Mg# and TiO_2, Al_2O_3, Cr_2O_3, and

Na_2O contents. The outer cores show intermediate compositions between the inner extremely low-Mg# cores and the high-Mg# mantles (Fig. 6). However, both inner cores and outer cores show the same REE patterns, implying the same origin. The intermediate compositions of outer cores may be the results of compositional diffusion between the inner cores and high-Mg# mantles (e.g., Dimanov and Wiedenbeck 2006; Mollo et al. 2010). Meanwhile, the cores are compositionally similar to the Cpx from high-pressure granulite in West Qinling (Fig. 9, Yang et al. 2018). Previous studies have demonstrated that the lower crust of West Qinling experienced granulite-facies metamorphism during the early Paleozoic (Mao et al. 2017; Oh and Lee 2019). Therefore, the Type–3 Cpx cores may be xenocrysts originating from high-pressure granulite. The mantles have identical major and trace compositions as the Type–1 Cpx cores and Type–2 Cpx mantles, indicating that the mantles also crystallized from a later primitive alkali magma that is cognate with the host magma.

The compositions of Type 1–3 Cpx rims differ significantly from those in adjacent cores or mantles (Fig. 5), which suggest that the rims overgrew the spongy cores or mantles after a new batch entered the magma reservoir (Grant et al. 2013). Besides, all the rims have identical compositions, similar to the Cpx orthocrysts, indicating they crystallized from the latest batch of host magma.

Combining all the evidence discussed above, we conclude that the Type–1 Cpx cores are antecrysts that crystallized from an early batch of primitive magma; they then entered the host magma to form the low-Mg# rims, which led to the normal zoning texture. The Type–2 Cpx core-mantle parts are antecrysts. We speculate that the low-

Mg# Type–2 Cpx cores grew in a chemically stable magma mush, where continuous supplement of uniformly evolved magma caused the growth of large cores. Subsequently, the recharge of more primitive alkali magma formed the high-Mg# mantles. Finally, the core-mantle parts were incorporated into the host magma where the rims crystallized, resulting in the formation of the simple oscillatory zoning. The Type–3 Cpx cores are xenocrysts from high-pressure granulites; these cores were captured by a primitive alkali magma where their high-Mg# mantles crystallized, and the Type–3 Cpx core-mantle parts entered the host magma to grow the rims, resulting in a complex oscillatory zoning. The Type–4 Cpx are orthocrysts, which crystallized from the host magma.

The origin of the spongy textures in the Cpx antecrysts/xenocrysts

In Type–1 and Type–2 Cpx, the sieves are mainly concentrated in the core and mantle parts, respectively. The diameters of the sieves in these Cpx are generally larger than 15 μm, and the spongy spaces are filled with the mineral assemblage K-feldspar and ilmenite (Fig. 7). In Type–3 Cpx, the sieves are mainly distributed in the high-Mg# mantles and generally have small diameters, only mineral assemblages in the sieves with slightly larger sizes (also K-feldspar and ilmenite) can be identified (Fig. 7i-k).

Mineral textures and associated compositional variations can provide crucial information on the crystal-melt/fluid interactions in a magma reservoir (e.g., Fowler 1995; Streck 2008; Zheng et al. 2005; Zhang 2005; Zhang et al. 2007; Jankovics et al. 2019). The proposed formation mechanisms for the spongy texture include (1) the interaction of the xenolith with the host magma during ascension (Shaw et al. 2006; Liu et al. 2012), (2) mantle metasomatism, i.e., the rock-melt/fluid interaction at depth (Coltorti et al. 1999), (3) incongruent partial melting induced by fluid penetration (Carpenter et al. 2002; Guzmics et al. 2008), and (4) decompression-induced partial melting (Su et al. 2011; Pan et al. 2018).

Mantle metasomatism processes always occur as peridotite–melt/fluid interaction and are frequently used to account for the formation of spongy texture in mantle minerals, such as clinopyroxene and spinel (Su et al. 2011). However, there is a lack of evidence to confirm the crystallization of Cpx in Majuangou alkali basalts at the mantle depths. Additionally, we did not observed any residual melt pockets or metasomatic melts near the spongy zones in Cpx, which are considered as good indicators of the mantle metasomatism (Carpenter et al. 2002; Su et al. 2011). Therefore, the formation of the spongy textures in Type 1–3 Cpx cannot be ascribed to metasomatic processes.

Previous studies revealed a significant Na_2O, Al_2O_3, and FeO depletion in "spongy" Cpx formed by partial melting relative to "intact" Cpx (Carpenter et al. 2002; Guzmics et al. 2008). Furthermore, incongruent partial melting could produce low-Na, high-Ca Cpx (e.g., Hibbard and Sjoberg 1994). The spongy zones of the Cpx in our Majuangou samples do not exhibit such characteristics. Rather, they have higher or comparable Na_2O but lower CaO contents than "intact" Cpx rims (Fig. 5). The literature regards plagioclase, olivine, titaniferous magnetite, ilmenite, and amorphous glass within clinopyroxene sieves as products of partial melting (Hibbard and Sjoberg 1994; Su et al. 2011; Pan et al. 2018). However, EDS analysis confirmed that K-feldspar and ilmenite fill the sieves in our Cpx, which are unlikely products of partial melting,

DOI: https://doi.org/10.2138/am-2022-8744. http://www.minsocam.org/

because the K_2O contents of Cpx are too low to form K-feldspar (Table S2). Moreover, the interfaces of the high-Mg# spongy zones that are immediately adjacent to the low-Mg# intact parts in Cpx are embayed, indicating that the spongy zones have reacted with melt or fluid. Consequently, the spongy textures are probably attributed to the interaction of Cpx with melt or fluid due to a local compositional disequilibrium. The spongy texture in the Cpx antecrysts/xenocrysts implies a possible reaction between the crystals and host magmas. The sieves in Cpx are filled with a mineral assemblage of K-feldspar and ilmenite, in contrast to the groundmass consisting of plagioclase, biotite, and ilmenite (Fig. 2c). These mineralogical characteristics indicate that the reaction between the host magmas and Cpx crystals may have produced K-feldspar and ilmenite at the expense of Cpx. However, if the reactants were only the host magmas and Cpx crystals and K-rich phases were lacking the reaction should not have produced K-feldspar. Therefore, the participation of K-rich substances was essential for the formation of K-feldspar. The biotite glomerocrysts in the groundmass (Fig. 2j-l) further prove the presence of K-rich components (in terms of melts or fluids) in the magmas.

Therefore, the mineral inclusion assemblage in the sieves confirms a chemical reaction. This reaction could have happened with the form of: melt 1 (primitive or evolved) + K-rich melt/fluid + Cpx ($CaMgSi_2O_6$) = K-feldspar ($KAlSi_3O_8$) + Ilmenite ($FeTiO_3$) + melt 2 (derivative), as manifested by the reaction between Cpx and alkali silicate melts (Sack and Carmichael 1984). Thus, we argue that the spongy texture and the mineral inclusions in the sieves were preserved as the products of the reaction between Cpx antecrysts or xenocrysts with the host melt/fluid.

Cpx-melt equilibrium and P-T constraints

Using Cpx-melt thermobarometers (equation T2 and P1 of Putirka et al., 1996), we estimate the crystallization temperatures and pressures for Type 1–4 Cpx and thus the depths of different magma reservoirs. However, the high-Mg# parts in Type 1–3 Cpx antecrysts or xenocrysts are in equilibrium with the host rocks while the Cpx orthocrysts are not (Fig. S3). Coote and Shane (2018) demonstrated that the whole-rock compositions can be modified by adding foreign materials. Petrographic observations reveal that our samples contain significant amounts of foreign Cpx, including 3-5% of Type–1 Cpx, approximately 2% of Type–2 Cpx, less than 1% of Type–3 Cpx, and 5% of pyroxenite xenoliths. Therefore, Fig. S3 sometimes shows a compositional pseudo-equilibrium between the whole-rock compositions and foreign crystals due to the high abundances of Cpx antecrysts/xenocrysts or pyroxenite xenoliths in the bulk rocks. Thus, the whole-rock compositions are unlikely to represent the initial equilibrium melts where either the orthocrysts, antecrysts, or xenocrysts crystallized.

The key to calculate the crystallization temperatures and pressures is to obtain the equilibrium melt compositions of Cpx, which may be inferred from the whole rock compositions (Neave and Putirka 2017). As mentioned above, the Cpx antecrysts or xenocrysts crystallized from melts (more primitive or evolved) cognate with the host melts, wherefore the addition or removal of mafic crystals (Cpx + Ol ± Pl) from the host-rock compositions can yield the equilibrium melts of foreign Cpx. Methodologically, we followed Armienti et al. (2013) and recalculated the compositions of the equilibrium melts of Cpx orthocrysts, antecrysts, or xenocrysts (except for the Type–3 Cpx cores with possible granulite origin) by moving backward (or forward) the whole-rock compositions along the cotectic path Cpx + Ol + Plg (Table S4). The host melts are assumed to have a Fe^{2+}/Fe_{tot} ratio of 0.9, corresponding to the FMQ buffer which is typical for basaltic magmas in non-arc settings (Neave and Putirka 2017).

The Fe-Mg exchange coefficient ($K_D^{Fe–Mg}$; estimated at 0.28±0.08 by Putirka 2008) is a common test for the equilibrium between Cpx and the host melt (Putirka et al. 1996, 1999). The comparison of the Cpx components (DiHd, EnFs, CaTs and Jd) obtained in clinopyroxene-melt equilibrium experiments with those observed in our Cpx is an additional test (Putirka 1999). To verify the Cpx-recalculated melt equilibrium, we compared $K_D^{Fe–Mg}$, DiHd, and EnFs, and if the values analyzed in Cpx and predicted for Cpx-recalculated melt pairs overlapped within 2σ uncertainty of the model, equilibrium was considered to have been met. The 1 standard error of estimate (SEE) used for the $K_D^{Fe–Mg}$, DiHd, and EnFs predicted values were ± 0.03, ± 0.06, and ± 0.05, respectively (Putirka 2008; Mollo et al. 2013), and the recalculated melts are in equilibrium with Cpx antecrysts, xenocrysts, and orthocrysts (Fig. S4).

The Cpx-recalculated melt pairs were used for the thermobarometer and yielded wide ranges of temperatures (1154–1308 °C) and pressures (3.14–15.70 kbar). The thermobarometer results may be separated into two distinct populations (Fig. 10a), (1) 1225–1308 °C, 9.49–15.70 kbar for the high-Mg# parts in Type 1–3 Cpx, (2) 1154–1220 °C, 3.14–9.79 kbar for the low-Mg# parts in Type 1–3 Cpx and Type–4 Cpx. Using the Gaussian model, the expected pressure values and standard deviations of the two populations are 8.14 kbar and 11.68 kbar (Fig. 10b&c). Consequently, two magma reservoirs existed in the Majuangou magmatic plumbing system at different depths of 30.1 km and 40.9 km, respectively (using the equation D [km]=5.35+3.04×P [kbar]; Sun et al., 2018). The high-Mg# cores and low-Mg# rims of Type–1 Cpx correspond to 10.00–15.70 kbar (most values are 10.00–13.66 kbar) and 8.31–9.48 kbar, respectively, indicting the cores formed in a deep magma chamber prior to entrainment into a new batch of evolved magma. Type–2 Cpx are characterized by the low-Mg# cores with crystallization pressures of 6.56–9.79 kbar (25.3–35.1 km). However, the high-Mg# mantles have higher crystallization pressures of 9.49–14.07 kbar than the cores. The thermobarometer of Putirka et al. (2003) also confirmed that the mantles experienced greater crystallization pressures of 9.55–14.94 kbar than the cores with 6.89–11.36 kbar. This suggests that the results of the thermobarometer calculations may be primarily influenced by the mineral composition, as a more primitive composition could lead to a higher crystallization pressure value. It is therefore untenable to rely exclusively on the results of thermobarometer to determin the crystallization depths of minerals. As mentioned above, the high-Mg# mantles of Type–2 Cpx formed due to recharge of mafic magma into a crystal mush. It seems to be not reasonable that the mantles have greater crystallization depths than the cores, and we propose that the mantles formed in a magma reservoir at a similar depth as the low-Mg# cores. Previous studies have reported similar crystal zoning patterns and explanations, with the high-Mg# mantles/rims of reversely zoned Cpx yielding higher crystallization pressures compared to the low-Mg# antecrystic cores (Coote and Shane 2018; Cao et al. 2022). The Type–

3 Cpx cores are thought to have a metamorphic origin and are not suitable for the application of the Cpx-melt thermobarometer. The high-Mg# mantles possess similar pressure values (11.93–15.11 kbar) as the high-Mg# parts of Type 1–2 Cpx. The metamorphic cores were captured by the high-Mg# magma during magma ascent, though we cannot directly estimate its crystallization pressures, their crystallization depths should be equal to or higher than the crystallization pressures of the Cpx mantles. Type–3 Cpx cores have identical compositions as the Cpx from high-pressure granulite in the same region, which formed at 13–15 kbar (Yang et al. 2018), corresponding to the depth (44.9–51.0 km) of the high-pressure granulite facies. Therefore, the Type–3 Cpx cores formed at high pressures and were captured by a batch of primitive magma before being overgrown by the high-Mg# mantles. Except for a few outliers, all the rims of Type 1–3 Cpx and Type–4 Cpx (Cpx orthocrysts) have uniform crystallization pressures (5.51–9.64 kbar), indicating they formed in the shallow magma reservoir at a depth of 30.1 km.

Details of the Cpx-host melt/fluid reaction and pre-eruptive process for magmatic plumbing system

The presence of Cpx crystals with various origins in the host magma demonstrates that the magmatic plumbing system has undergone complex dynamic processes, including the incorporation of previous igneous cumulates, the uptake of disaggregated fragments of crystal mushes, and the capture of lower crustal materials.

Given a crustal thickness of ~52 km beneath West Qinling (Zhang et al. 2020), the

DOI: https://doi.org/10.2138/am-2022-8744. http://www.minsocam.org/

Cpx-melt thermobarometry demonstrates that at least two lower crustal magma reservoirs were active in the magma plumbing system of the Majuangou area (Fig. 11). The deeper magma reservoir is located at a depth of ~40.9 km, consists of primitive magmas, and crystallized high-Mg# Cpx (Type–1 Cpx cores and Type–3 Cpx mantles). The shallower magma reservoir at a depth of ~30.1 km consists of multiple batches of low-Mg# magmas which formed and low-Mg# Cpx (Type–2 Cpx cores, Type 1–3 Cpx rims and Type–4 Cpx). The compositional and textural features of these Cpx crystals suggest at least three discrete batches of magmatic activity in the Majuangou alkali magmatic plumbing system (Fig. 12).

(1) The Batch-1 magma was long-lived and consisted of multiple batches of low-Mg# alkali magmas (Mg#: 47.4–53.3, Table S4). Continuous recharge of homogeneous magmas formed the magma mush where the Type–2 Cpx cores crystallized (Fig. 12). The resorbed characteristics of Type-2 Cpx cores may be the result of antecedent crystal dissolution caused by subsequent magmas.

(2) The Batch-2 primitive magma (Mg#: 57.2–64.5) stayed at the deeper magma reservoir, where the high-Mg# Type–1 Cpx cores (i.e., a type of antecryst) formed. Meanwhile, the Batch-2 magma also replenished the Batch-1 magma mush, in which Type–2 Cpx mantles crystallized. The Mg and Cr enrichments of Type–2 Cpx mantles (Fig. S2) verify this hot and mafic magma recharge (Ubide and Kamber 2018), which may trigger the reactivation of previous magma mush (Coote and Shane 2018). In addition, the Type–3 Cpx cores derived from high-pressure granulites were captured by the Batch-2 primitive magma, where the high-Mg# mantles subsequently overgrew (Fig.

12). The compositional diffusion from Type-3 Cpx mantles results in the differentiation of cores, forming the inner cores with unchanged compositions and outer cores with intermediate compositions (Fig. 5).

(3) The ensuing magma batch (i.e., Batch–3 low-Mg# magma with Mg# of 47.2–54.6 after remove an outlier of 42.0) passed through the magma reservoir where the Batch–2 primitive magma was stored during ascent, and took away the previously crystallized Cpx as antecrysts. The Batch-3 magma migrated upward and assembled all the above-mentioned crystals (antecrysts or xenocrysts) in the shallow host magma reservoir, further crystallized Type 1–3 Cpx rims (Fig. 12) and Type–4 Cpx. These Cpx antecrysts/xenocrysts reacted with the Batch-3 magma due to compositional disequilibrium, and formed the observed spongy textures. K-feldspar and ilmenite as the products of reaction filled the sieves of spongy zones.

(4) The rims of Cpx antecrysts or xenocrysts (Type 1–3 Cpx) may have formed during the final stage of host magma undercooling, which is supported by the observation that these rims have more evolved compositions (i.e., low Mg#) than the Type–4 Cpx (Fig. 5). All these Cpx antecrysts/xenocrysts were ultimately carried to the surface by the eruption.

The similarity of the REE patterns between the high-Mg# parts and the low-Mg# parts (except for the extremely low-Mg# cores of Type–3 Cpx) in all types of Cpx (Type 1–4 Cpx) demonstrates that these different batches of alkali magmas have a cognate relationship (Fig. 8). When the host magma captured these foreign Cpx crystals, the compositional disequilibrium between the crystals and the magmas might have caused

DOI: https://doi.org/10.2138/am-2022-8744. http://www.minsocam.org/

resorption (dissolution) and reaction between the Cpx and host magmas.

Implications

A simple magmatic plumbing system, consisting of a single magma reservoir and a magma conduit, cannot explain the diversity of mineral zoning patterns and the complexity of Cpx origins in the Majuangou alkali basalts. In contrast, the Cpx crystals with various origins and zoning textures in Cenozoic basalts from West Qinling have demonstrated that the basaltic plumbing system was fed by complex, multiple batches of magma pulses from magma reservoirs at various depths. These spatially related magma reservoirs are interconnected by magma conduits, thus resulting in a complicated, multistage trans-crustal magmatic plumbing system. The later batches of magma rose along the conduits, carried crystals from different magma reservoirs into the shallow magma reservoir, from where they ultimately erupted to the surface. This magmatic plumbing system has a complex magmatic evolutionary history, manifested by the various textural and compositional characteristics of clinopyroxenes.

The zoning textures of Cpx antecrysts or xenocrysts faithfully record the evolution of the parent magmas and thus provide crucial evidence on the cryptic magma mixing/recharging, which neither the whole-rock Sr-Nd-Pb isotopic compositions nor mineral in-situ Sr isotopes can reflect, if their discrete parent magma batches are cognate. The reactions between antecrysts or xenocrysts and their host magmas are driven by compositional disequilibrium, resulting in the spongy textures within the minerals. Furthermore, the spongy textures can provide insight into the details of

DOI: https://doi.org/10.2138/am-2022-8744. http://www.minsocam.org/

crystal-melt/fluid reactions and the nature of reacting melts/fluids (Shaw et al. 2005, 2006; Zhang et al. 2007). The new insights we have obtained differ from previous studies holding the view that the crystal-melt/fluid reactions require cracks in the minerals, which as channels, facilitate the injection of melt and increase the contact surface (cf., Shaw et al. 2006; Xing and Wang 2020). Contrary to the previous viewpoint, we conclude that the crystal-melt/fluid reaction can occur without the presence of cracks, which is supported by the fact that the spongy textures of Cpx antecrysts/xenocrysts are not coupled to the distribution of cracks. Different scales of spongy zones may primarily depend on the reaction time between crystals and melts/fluids.

The incorporation of considerable numbers of Cpx antecrysts/xenocrysts into host magmas (e.g., the proportion of foreign Cpx exceeding 10% in our samples) can significantly modify the whole-rock compositions, especially the Mg and Fe contents. This modification can cause the host magmas to evolve towards equilibrium with foreign Cpx crystals, even resulting in a compositional pseudo-equilibrium. Therefore, to determine whether clinopyroxene and host melt are in equilibrium by first using the Mg-Fe exchange coefficient to distinguish the origins of Cpx (foreign crystal or orthocryst) and afterwards calculating the crystallization temperature, pressure, and H_2O content may lead to incorrect judgments and calculation results. Crystal-melt/fluid reactions may also contribute to the magmatic evolution by consuming Mg and Fe components in the host magmas. The potential influence of the incorporation of foreign crystals must be considered, when the whole-rock compositions are used to determine a crystal-melt equilibrium or to calculate mineral crystallization temperatures and pressures.

Acknowledgments

We are greatlt grateful to editor Hong-Wu Xu and associate editor Callum Hetherington for their efficient handling and valuable comments. We also thank reviewers Ruadhan Magee and Alice MacDonald for their constructive comments which have contributed to improve the manuscript. This work was jointly funded by the State Key Program of National Natural Science of China (Grant No. 41730426) and the National Natural Science Foundation of China (Grant Nos. 41872066 and 41702069), the Fundamental Research Funds for the Central Universities of China (Grant No. 2652019054, 2652019323 and 2652018121), and the Open Research Funds for GPMR (Grant GPMR201509).

References

Armienti, P., Perinelli, C., and Putirka, K.D. (2013) A new model to estimate deep-level magma ascent rates, with applications to Mt. Etna (Sicily, Italy). Journal of Petrology, 54(4), 795–813.

Bach, P., Smith, I., and Malpas, J. (2012) The origin of garnets in andesitic rocks from the Northland Arc, New Zealand, and their implication for sub-arc processes. Journal of Petrology, 53(6), 1169–1195.

BAS, M.L., Maitre, R.L., Streckeisen, A., and Zanettin, B. (1986) A chemical classification of volcanic rocks based on the total alkali-silica diagram. Journal of petrology, 27(3), 745–750.

Cao, G., Xue, H., and Tong, Y. (2022) Complex magmatic processes recorded by clinopyroxene phenocrysts in a magmatic plumbing system: A case study of mafic volcanic rocks from the Laiyang Basin, southeastern North China Craton. Lithos, 106673.

Carpenter, R., Edgar, A., and Thibault, Y. (2002) Origin of spongy textures in clinopyroxene and spinel from mantle xenoliths, Hessian Depression, Germany. Mineralogy and Petrology, 74(2–4), 149–162.

Cashman, K., and Blundy, J. (2013) Petrological cannibalism: The chemical and textural consequences of incremental magma body growth. Contributions to Mineralogy and Petrology, 166(3), 703–729.

Cashman, K.V., Sparks, R.S.J., and Blundy, J.D. (2017) Vertically extensive and unstable magmatic systems: a unified view of igneous processes. Science, 355(6331).

Coltorti, M., Bonadiman, C., Hinton, R., Siena, F., and Upton, B. (1999) Carbonatite metasomatism of the oceanic upper mantle: Evidence from clinopyroxenes and glasses in ultramafic xenoliths of Grande Comore, Indian Ocean. Journal of Petrology, 40(1), 133–165.

Coote, A., and Shane, P. (2018) Open-system magmatic behaviour beneath monogenetic volcanoes revealed by the geochemistry, texture and thermobarometry of clinopyroxene, Kaikohe-Bay of Islands volcanic field (New

Zealand). Journal of Volcanology and Geothermal Research, 368, 51–62.

Cristina, P., Mario, G., Barbara, B., Serena, F.G., Carmela, F., Vincenzo, S., Stefania, S., and Claudia, R. (2019) Effect of water on the phase relations of primitive K-basalts: Implications for high-pressure differentiation in the Phlegraean Volcanic District magmatic system. Lithos, 342, 530–541.

Dimanov, A., and Wiedenbeck, M. (2006) (Fe, Mn)-Mg interdiffusion in natural diopside: Effect of pO_2. European Journal of Mineralogy, 18(6), 705–718.

Dong, Y., Genser, J., Neubauer, F., Zhang, G., Liu, X., Yang, Z., and Heberer, B. (2011) U-Pb and $^{40}Ar/^{39}Ar$ geochronological constraints on the exhumation history of the North Qinling terrane, China. Gondwana Research, 19(4), 881–893.

Edmonds, M., Cashman, K.V., Holness, M., and Jackson, M. (2019) Architecture and dynamics of magma reservoirs, 377, p. 20180298. The Royal Society Publishing.

Elardo, S.M., and Shearer, C.K., Jr. (2014) Magma chamber dynamics recorded by oscillatory zoning in pyroxene and olivine phenocrysts in basaltic lunar meteorite Northwest Africa 032. American Mineralogist, 99(2–3), 355–368.

Feng, W., and Zhu, Y. (2018) Decoding magma storage and pre-eruptive processes in the plumbing system beneath early Carboniferous arc volcanoes of southwestern Tianshan, Northwest China. Lithos, 322, 362–375.

Feng, W., and Zhu, Y. (2019) Magmatic plumbing system beneath a fossil continental arc volcano in western Tianshan (NW China): Constraints from clinopyroxene and thermodynamic modelling. Lithos, 350, 105221.

Fowler, A. (1995) Mineral crystallinity in igneous rocks. Fractals in the earth sciences,

p. 237–249. Springer.

Francalanci, L., Braschi, E., Di Salvo, S., Lucchi, F., and Petrone, C.M. (2014) When magmas do not interact: Paired Roman-age activity revealed by tephra studies at Stromboli volcano. Bulletin of Volcanology, 76(12), 884.

Frey, F.A., and Prinz, M. (1978) Ultramafic inclusions from San Carlos, Arizona: Petrologic and geochemical data bearing on their petrogenesis. Earth and Planetary Science Letters, 38(1), 129–176.

Ganne, J., Bachmann, O., and Feng, X. (2018) Deep into magma plumbing systems: Interrogating the crystal cargo of volcanic deposits. Geology, 46(5), 415–418.

Giacomoni, P.P., Coltorti, M., Bryce, J., Fahnestock, M., and Guitreau, M. (2016) Mt. Etna plumbing system revealed by combined textural, compositional, and thermobarometric studies in clinopyroxenes. Contributions to Mineralogy and Petrology, 171(4), 34.

Ginibre, C., Kronz, A., and Wörner, G. (2002) High-resolution quantitative imaging of plagioclase composition using accumulated backscattered electron images: New constraints on oscillatory zoning. Contributions to Mineralogy and Petrology, 142(4), 436–448.

Ginibre, C., Wörner, G., and Kronz, A. (2007) Crystal zoning as an archive for magma evolution. Elements, 3(4), 261–266.

Grant, T.B., Milke, R., Pandey, S., and Jahnke, H. (2013) The Heldburg Phonolite, Central Germany: Reactions between phonolite and xenocrysts from the upper mantle and lower crust. Lithos, 182, 86–101.

Guo, P., Niu, Y., and Yu, X. (2014) A synthesis and new perspective on the petrogenesis of kamafugites from West Qinling, China, in a global context. Journal of Asian Earth Sciences, 79, 86–96.

Guzmics, T., Kodolányi, J., Kovács, I., Szabó, C., Bali, E., and Ntaflos, T. (2008) Primary carbonatite melt inclusions in apatite and in K-feldspar of clinopyroxene-rich mantle xenoliths hosted in lamprophyre dikes (Hungary). Mineralogy and Petrology, 94(3–4), 225.

Hibbard, M., and Sjoberg, J.J. (1994) Signs of incongruent melting of clinopyroxene in limburgite, Thetford Hill, Vermont. The Canadian Mineralogist, 32(2), 307–317.

Jankovics, M.É., Sági, T., Astbury, R.L., Petrelli, M., Kiss, B., Ubide, T., Németh, K., Ntaflos, T., and Harangi, S. (2019) Olivine major and trace element compositions coupled with spinel chemistry to unravel the magmatic systems feeding monogenetic basaltic volcanoes. Journal of Volcanology and Geothermal Research, 369, 203–223.

Jerram, D.A., and Martin, V.M. (2008) Understanding crystal populations and their significance through the magma plumbing system. Geological Society, London, Special Publications, 304(1), 133–148.

Li, X., Mo, X., Huang, X., Dong, G., Yu, X., Luo, M., and Liu, Y. (2015) U-Pb zircon geochronology, geochemical and Sr–Nd–Hf isotopic compositions of the Early Indosinian Tongren Pluton in West Qinling: Petrogenesis and geodynamic implications. Journal of Asian Earth Sciences, 97, 38–50.

Li, X., Zeng, Z., Yang, H., Zhao, Y., Yin, X., Wang, X., Chen, S., Qi, H., and Guo, K.

(2020) Integrated major and trace element study of clinopyroxene in basic, intermediate and acidic volcanic rocks from the middle Okinawa Trough: Insights into petrogenesis and the influence of subduction component. Lithos, 352, 105320.

Liu, C.-Z., Wu, F.-Y., Sun, J., Chu, Z.-Y., and Qiu, Z.-L. (2012) The Xinchang peridotite xenoliths reveal mantle replacement and accretion in southeastern China. Lithos, 150, 171–187.

Liu, D., Zhao, Z., Niu, Y., Zhu, D.-C., and Li, X.-H. (2018) Perovskite U-Pb and Sr-Nd isotopic perspectives on melilitite magmatism and outward growth of the Tibetan Plateau. Geology, 46(12), 1027–1030.

Liu, Y., Hu, Z., Gao, S., Günther, D., Xu, J., Gao, C., and Chen, H. (2008) In situ analysis of major and trace elements of anhydrous minerals by LA-ICP-MS without applying an internal standard. Chemical Geology, 257(1–2), 34–43.

Lucci, F., Carrasco-Núñez, G., Rossetti, F., Theye, T., White, J.C., Urbani, S., Azizi, H., Asahara, Y., and Giordano, G. (2020) Anatomy of the magmatic plumbing system of Los Humeros Caldera (Mexico): Implications for geothermal systems. Solid Earth, 11(1), 125–159.

Luo, B., Zhang, H., Xu, W., Yang, H., Zhao, J., Guo, L., Zhang, L., Tao, L., Pan, F., and Gao, Z. (2018) The magmatic plumbing system for Mesozoic high-Mg andesites, garnet-bearing dacites and porphyries, rhyolites and leucogranites from West Qinling, central China. Journal of Petrology, 59(3), 447–482.

Ma, G.S.-K., Wang, K.-L., Malpas, J., Iizuka, Y., Xenophontos, C., Turkmani, A.A., Chan, G.H.-N., Usuki, T., and Chan, Q.H.-S. (2015) Melt pockets and spongy clinopyroxenes in mantle xenoliths from the Plio-Quaternary Al Ghab volcanic field, NW Syria: Implications for the metasomatic evolution of the lithosphere. The Earth's Heterogeneous Mantle, p. 205–257. Springer.

Magee, C., Stevenson, C.T., Ebmeier, S.K., Keir, D., Hammond, J.O., Gottsmann, J.H., Whaler, K.A., Schofield, N., Jackson, C.A., and Petronis, M.S. (2018) Magma plumbing systems: A geophysical perspective. Journal of Petrology, 59(6), 1217–1251.

Magee, R., Ubide, T., and Caulfield, J. (2021) Days to weeks of syn-eruptive magma interaction: High-resolution geochemistry of the 2002-03 branched eruption at Mount Etna. Earth and Planetary Science Letters, 565, 116904.

Mao, X., Zhang, J., Yu, S., Li, Y., Yu, X., and Lu, Z. (2017) Early Paleozoic granulite-facies metamorphism and anatexis in the northern West Qinling orogen: Monazite and zircon U-Pb geochronological constraints. Science China Earth Sciences, 60(5), 943–957.

Masotta, M., Pontesilli, A., Mollo, S., Armienti, P., Ubide, T., Nazzari, M., and Scarlato, P. (2020) The role of undercooling during clinopyroxene growth in trachybasaltic magmas: Insights on magma decompression and cooling at Mt. Etna volcano. Geochimica et Cosmochimica Acta, 268, 258–276.

Miller, J.S., Matzel, J.E., Miller, C.F., Burgess, S.D., and Miller, R.B. (2007) Zircon growth and recycling during the assembly of large, composite arc plutons. Journal of Volcanology and Geothermal Research, 167(1–4), 282–299.

Milman-Barris, M.S., Beckett, J.R., Baker, M.B., Hofmann, A.E., Morgan, Z., Crowley, M.R., Vielzeuf, D., and Stolper, E. (2008) Zoning of phosphorus in igneous olivine. Contributions to Mineralogy and Petrology, 155(6), 739–765.

Mollo, S., Del Gaudio, P., Ventura, G., Iezzi, G., and Scarlato, P. (2010) Dependence of clinopyroxene composition on cooling rate in basaltic magmas: Implications for thermobarometry. Lithos, 118(3–4), 302–312.

Mollo, S., Putirka, K., Misiti, V., Soligo, M., and Scarlato, P. (2013) A new test for equilibrium based on clinopyroxene–melt pairs: Clues on the solidification temperatures of Etnean alkaline melts at post-eruptive conditions. Chemical Geology, 352, 92–100.

Morimoto, N., Fabries, J., Fergunson, A., Ginzburg, I., Ross, M.S., and FA, Z. J., Aoki, K. y Gottardi, G. (1988). American. Mineralogist, 73, 1123–1133.

Müller, T., Dohmen, R., Becker, H., Ter Heege, J.H., and Chakraborty, S. (2013) Fe-Mg interdiffusion rates in clinopyroxene: Experimental data and implications for Fe-Mg exchange geothermometers. Contributions to Mineralogy and Petrology, 166(6), 1563–1576.

Neave, D.A., and Putirka, K.D. (2017) A new clinopyroxene-liquid barometer, and implications for magma storage pressures under Icelandic rift zones. American Mineralogist, 102(4), 777–794.

Oh, C.W., and Lee, B.C. (2019) The relationship between systematic metamorphic patterns and collisional processes along the Qinling–Sulu–Odesan collisional belt between the North and South China Cratons. Geological Society, London, Special Publications, 478(1), 449–475.

Pan, S., Zheng, J., Yin, Z., Griffin, W., Xia, M., Lin, A., and Zhang, H. (2018) Spongy texture in mantle clinopyroxene recordsdecompression-induced melting. Lithos, 320, 144–154.

Petrone, C.M., Braschi, E., Francalanci, L., Casalini, M., and Tommasini, S. (2018) Rapid mixing and short storage timescale in the magma dynamics of a steady-state volcano. Earth and Planetary Science Letters, 492, 206–221.

Pontesilli, A., Brenna, M., Ubide, T., Mollo, S., Masotta, M., Caulfield, J., Le Roux, P., Nazzari, M., Scott, J., and Scarlato, P. (2021) Intraplate basalt alkalinity modulated by a lithospheric mantle filter at the Dunedin Volcano (New Zealand). Journal of Petrology, 62(10), egab062.

Putirka, K. (1999) Clinopyroxene + liquid equilibria to 100 kbar and 2450 K. Contributions to Mineralogy and Petrology, 135(2), 151–163.

Putirka, K., Johnson, M., Kinzler, R., Longhi, J., and Walker, D. (1996) Thermobarometry of mafic igneous rocks based on clinopyroxene-liquid equilibria, 0-30 kbar. Contributions to Mineralogy and Petrology, 123(1), 92–108.

Putirka, K.D. (2008) Thermometers and barometers for volcanic systems. Reviews in mineralogy and geochemistry, 69(1), 61–120.

Putirka, K.D., Mikaelian, H., Ryerson, F., and Shaw, H. (2003) New clinopyroxene-liquid thermobarometers for mafic, evolved, and volatile-bearing lava compositions, with applications to lavas from Tibet and the Snake River Plain, Idaho. American Mineralogist, 88(10), 1542–1554.

Sack, R.O., and Carmichael, I.S.E. (1984) $Fe^{2}\rightleftarrows Mg^{2}$ and $TiAl_2\rightleftarrows MgSi_2$ exchange reactions between clinopyroxenes and silicate melts. Contributions to Mineralogy and Petrology, 85(2), 103–115.

Shaw, C.S., Heidelbach, F., and Dingwell, D.B. (2006) The origin of reaction textures in mantle peridotite xenoliths from Sal Island, Cape Verde: The case for "metasomatism" by the host lava. Contributions to Mineralogy and Petrology, 151(6), 681.

Shore, M., and Fowler, D. (1996) Oscillatory zoning in minerals, a common phenomenon. Canadian Mineralogist, 34, 1111–1126.

Streck, M.J. (2008) Mineral textures and zoning as evidence for open system processes. Reviews in Mineralogy and Geochemistry, 69(1), 595–622.

Su, B.-X., Zhang, H.-F., Sakyi, P.A., Yang, Y.-H., Ying, J.-F., Tang, Y.-J., Qin, K.-Z., Xiao, Y., Zhao, X.-M., and Mao, Q. (2011) The origin of spongy texture in minerals of mantle xenoliths from the Western Qinling, central China. Contributions to Mineralogy and Petrology, 161(3), 465–482.

Su, B.-X., Zhang, H.-F., Sakyi, P.A., Ying, J.-F., Tang, Y.-J., Yang, Y.-H., Qin, K.-Z., Xiao, Y., and Zhao, X.-M. (2010) Compositionally stratified lithosphere and carbonatite metasomatism recorded in mantle xenoliths from the Western Qinling (Central China). Lithos, 116(1–2), 111–128.

Su, B.-X., Zhang, H.-F., Ying, J.-F., Tang, Y.-J., Hu, Y., and Santosh, M. (2012) Metasomatized lithospheric mantle beneath the western Qinling, Central China: Insight into carbonatite melts in the mantle. The Journal of Geology, 120(6), 671–681.

Sun, P., Niu, Y., Guo, P., Cui, H., Ye, L., and Liu, J. (2018) The evolution and ascent paths of mantle xenolith-bearing magma: Observations and insights from Cenozoic basalts in Southeast China. Lithos, 310, 171–181.

Sun, S.-S., and McDonough, W.F. (1989) Chemical and isotopic systematics of oceanic basalts: implications for mantle composition and processes. Geological Society, London, Special Publications, 42(1), 313–345.

Turbeville, B. (1992) Relationships between chamber margin accumulates and pore liquids: evidence from arrested in situ processes in ejecta, Latera caldera, Italy. Contributions to Mineralogy and Petrology, 110(4), 429-441.

Ubide, T., Caulfield, J., Brandt, C., Bussweiler, Y., Mollo, S., Di Stefano, F., Nazzari, M., and Scarlato, P. (2019a) Deep Magma Storage Revealed by Multi-Method Elemental Mapping of Clinopyroxene Megacrysts at Stromboli Volcano. Frontiers in Earth Science, 7(239).

Ubide, T., and Kamber, B.S. (2018) Volcanic crystals as time capsules of eruption history. Nature communications, 9(1), 326.

Ubide, T., Mollo, S., Zhao, J.-X., Nazzari, M., and Scarlato, P. (2019b) Sector-zoned clinopyroxene as a recorder of magma history, eruption triggers, and ascent rates. Geochimica et Cosmochimica Acta, 251, 265–283.

Ubide, T., Neave, D.A., Petrelli, M., and Longpré, M.-A. (2021) Crystal archives of magmatic processes. Frontiers in Earth Science, 722.

van Gerve, T., Neave, D., Almeev, R., Holtz, F., and Namur, O. (2020) Zoned crystal records of transcrustal magma transport, storage and differentiation: Insights from the Shatsky Rise oceanic plateau. Journal of Petrology.

Wang, F., Ge, G., Ning, S., Nie, L., Zhong, G., and C, W.N. (2017) A new approach to LA-ICP-MS mapping and application in geology. Acta Petrologica Sinica, 33(11), 3422–3436.

Xing, C.-M., and Wang, C.Y. (2020) Periodic Mixing of Magmas Recorded by Oscillatory Zoning of the Clinopyroxene Macrocrysts from an Ultrapotassic Lamprophyre Dyke. Journal of Petrology, 61(11–12).

Yang, L., Song, S., Su, L., Li, Y., Dong, J., and Li, Q. (2018) Discovery of Liziyuan high-pressure granulite in Tianshui region: Evidence for Late Devonian orogeny in West Qinling Orogen. Acta Petrologica Sinica, 34(8), 2425–2440.

Yu, X.-H., Mo, X.-X., Zhao, Z.-D., He, W.-Y., and Li, Y. (2011) Cenozoic bimodal volcanic rocks of the West Qinling: Implication for genesis and nature of the rifting of north-south tectonic belt. Acta Petrologica Sinica, 27(7), 2195–2202.

Yu, X., Mo, X., Zhao, Z., Huang, X., Li, Y., Chen, Y., and Wei, Y. (2009) Two types of Cenozoic potassic volcanic rocks in West Qinling, Gansu Province: Their petrology, geochemistry and petrogenesis. Earth Science Frontiers, 16(2), 79–89.

Zhang, C., Guo, Z., and Chen, Y.J. (2020) Lithospheric thickening controls the ongoing growth of northeastern Tibetan Plateau: Evidence from P and S receiver functions. Geophysical Research Letters, 47(15), e2020GL088972.

Zhang, H.-F. (2005) Transformation of lithospheric mantle through peridotite-melt reaction: a case of Sino-Korean craton. Earth and Planetary Science Letters, 237(3–4), 768–780.

Zhang, H.-F., Ying, J.-F., Shimoda, G., Kita, N.T., Morishita, Y., Shao, J.-A., and Tang, Y.-J. (2007) Importance of melt circulation and crust-mantle interaction in the lithospheric evolution beneath the North China Craton: Evidence from Mesozoic basalt-borne clinopyroxene xenocrysts and pyroxenite xenoliths. Lithos, 96(1), 67–89.

Zheng, J., O'Reilly, S.Y., Griffin, W., Lu, F., Zhang, M., and Pearson, N. (2001) Relict refractory mantle beneath the eastern North China block: Significance for lithosphere evolution. Lithos, 57(1), 43–66.

Zheng, J., Zhang, R.Y., Griffin, W., Liou, J., and O'Reilly, S.Y. (2005) Heterogeneous and metasomatized mantle recorded by trace elements in minerals of the Donghai garnet peridotites, Sulu UHP terrane, China. Chemical Geology, 221(3–4), 243–259.

Figure Captions

Figure 1. (a) Topographic map of northeastern Tibetan Plateau (after Liu et al. 2018); (b) Location of the Majuangou volcanic cinder cone in West Qinling.

Figure 2. Hand specimens and photomicrographs of Majuangou alkali basalts. (a) Mantle peridotite xenoliths in alkali basalts; (b) The alkali basalts exhibit a porphyritic texture with large Ol and Cpx crystals and a plagioclase-dominated groundmass; (c) The groundmass has an intergranular texture and consists of euhedral plagioclase, interstitial Cpx, and minor olivine and ilmenite; (d) Type–1 Cpx crystals, with spongy cores surrounded by clean rims; (e) Type–2 Cpx crystals, which consist of cores, spongy

DOI: https://doi.org/10.2138/am-2022-8744. http://www.minsocam.org/

mantles, and clean rims, with frequently developed fractures; (f) Type–3 Cpx crystals are smaller than Type–2 Cpx, and consist of intact cores, spongy mantles, and clean rims; (g–i) BSE images of Type–1, Type–2, and Type–3 Cpx; the sieves in the spongy zones are filled by the mineral assemblage of K-feldspar and ilmenite. (j) Biotite glomerocrysts in the groundmass, plane-polarized light; (k) Biotite is distributed around Cpx glomerocrysts, plane-polarized light; (l) Same as (k), but in cross-polarized light. Ol = olivine; Cpx = clinopyroxene; Pl = plagioclase; Ilm = ilmenite; Kfs = K-feldspar.

Figure 3. $CaSiO_3$–$MgSiO_3$–$FeSiO_3$ diagram with the compositions of the Cpx crystals in Majuangou alkali basalts.

Figure 4. Textures and zoning patterns of Type 1–3 Cpx in Majuangou samples: (a) Type–1 Cpx shows normal zoning; (b) Type–2 Cpx exhibits simple oscillatory zoning; (c) Type–3 Cpx shows complex oscillatory zoning; Type–4 Cpx, suggested to be orthocrysts, are unzoned.

Figure 5. Binary plots of Mg# vs. SiO_2 (a), CaO (b), Al_2O_3 (c) and TiO_2 (d) contents of Cpx orthocrysts and Cpx xenocrysts/antecrysts of Majuangou samples. The legends are the same as in Figure 3.

Figure 6. (a) Compositional profiles of Type–1 Cpx, (b) Type–2 Cpx, (c) Type–3 Cpx; the white dashed line represents the transects which are analyzed. IC = Inner Core; OC = Outer Core.

Figure 7. BSE images and X-ray maps of Type 1–3 Cpx. (a-d) partial enlarged X-ray maps of Type–1 Cpx, the spongy cores are enclosed by clean rims; (e-h) partial enlarged X-ray maps of Type–2 Cpx, resorbed cores are enclosed by spongy mantles and further

surrounded by clean rims; (i-k) BSE photos of Type–3 Cpx (i) and partial enlarged drawing (j&k). The sieves in the spongy zones of Type 1–3 Cpx are filled with K-Feldspar and ilmenite.

Figure 8. (a) Chondrite-normalized REE patterns and (b) primitive mantle-normalized multiple elements distribution of Type 1–4 Cpx. The chondrite and primitive mantle values are from Sun and McDonough (1989).

Figure 9. Plots of Mg# vs. Na (a), Ca (b) (cations per formula unit based on ^{6}O). The number of cations were calculated by the method in Table 3 of Putirka (2008). Data sources: Cpx from mantle peridotite (Su et al. 2010, 2011) and granulite xenolith (Yang et al. 2018) in West Qinling. The legends are the same as in Figure 3.

Figure 10. (a) Temperatures and pressures calculated with the Cpx-melt thermobarometer; (b-c) Histograms and Gaussian density estimations of thermobarometry for high-Mg# (b) and low-Mg# Cpx (c). The symbols are the same as in Figure 3.

Figure 11. Conceptual model of the basaltic plumbing system beneath West Qinling. The Batch-1 magma consisted of multiple batches of low-Mg# alkali magmas, formed the magma mush containing the Type–2 Cpx cores; the Batch-2 magma was a hot and primitive magma, crystallized the Type–1 Cpx cores and replenished the magma mush; the Batch-3 low-Mg# magma passed through those magma reservoir during ascent, took away the previous Cpx, crystallized the rims of Type 1–3 Cpx and Type–4 Cpx.

Figure 12. Sketches for different batches of magmatic activity and their genetic relations with Type 1–3 Cpx.

This is the peer-reviewed, final accepted version for American Mineralogist, published by the Mineralogical Society of America.
The published version is subject to change. Cite as Authors (Year) Title. American Mineralogist, in press.
DOI: https://doi.org/10.2138/am-2022-8744. http://www.minsocam.org/

Figure 1

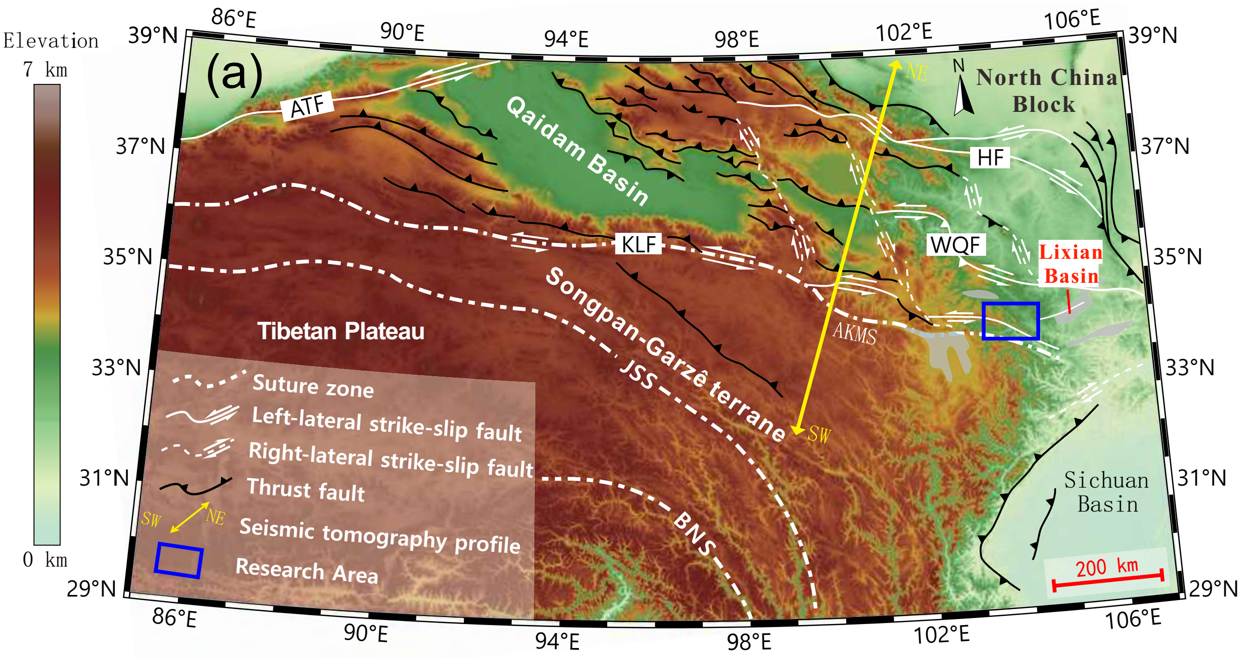

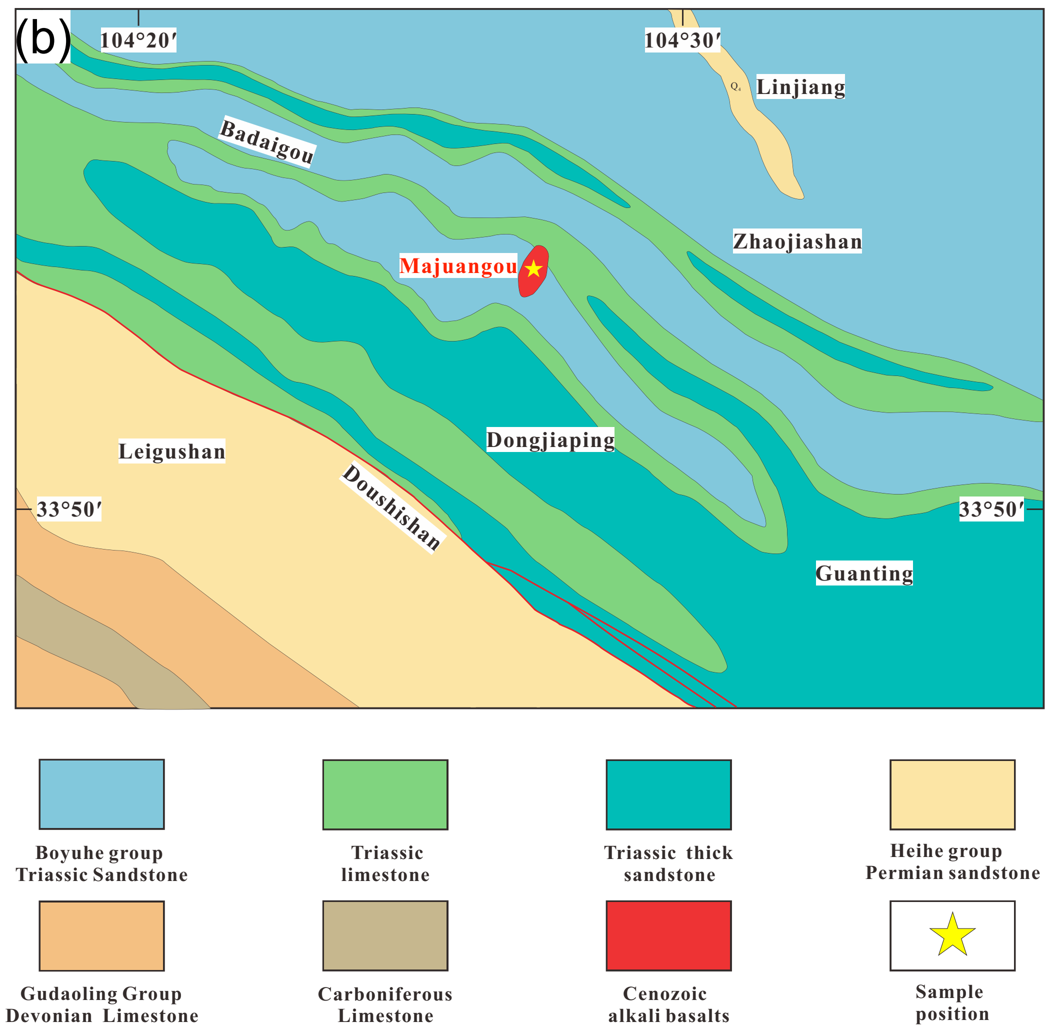

Figure 2

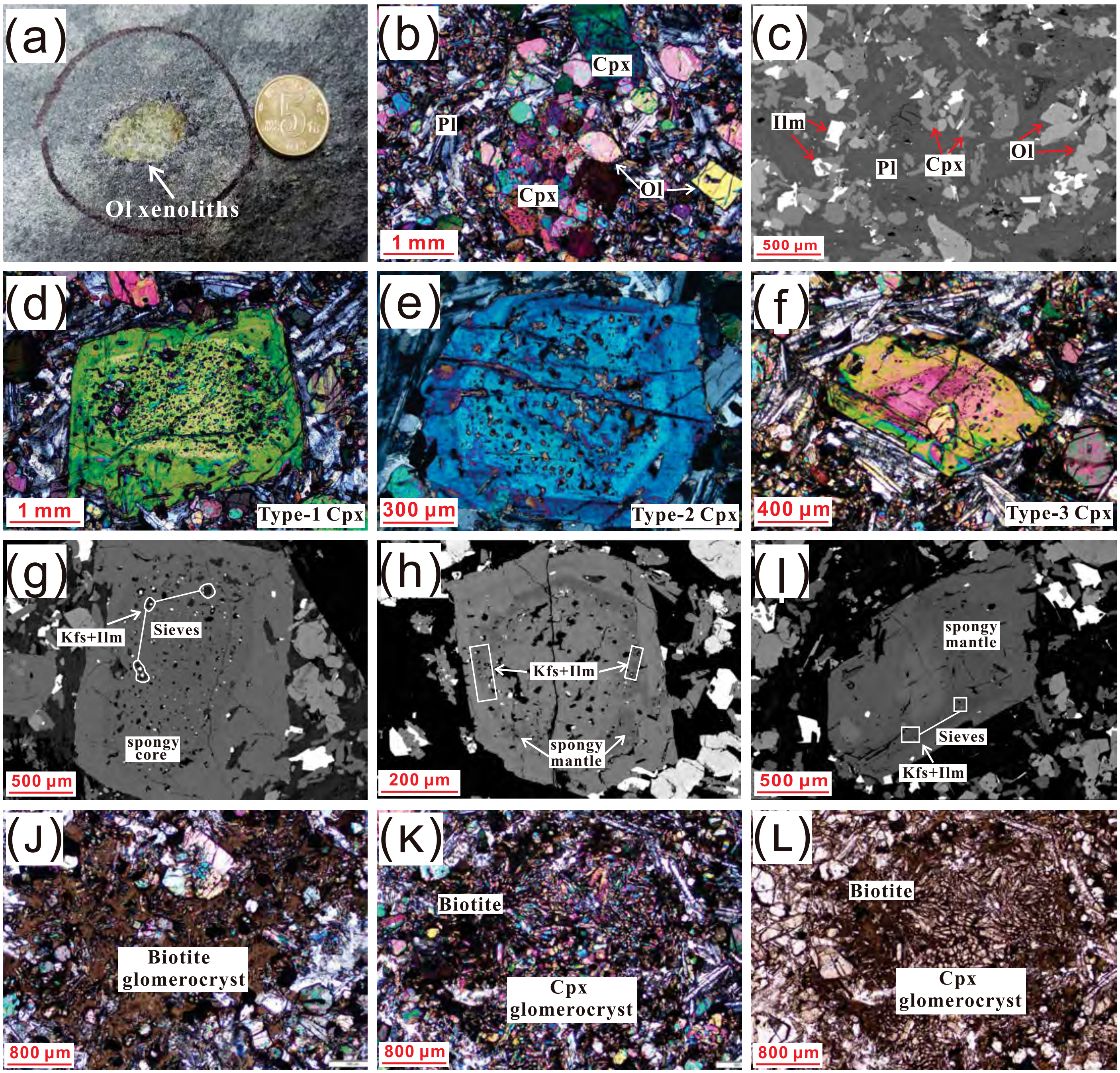
(a)
Ol xenoliths
(b)
Cpx
Pl
Cpx
Ol
1 mm
(c)
Ilm
Pl
Cpx
Ol
500 μm
(d)
1 mm
Type-1 Cpx
(e)
300 μm
Type-2 Cpx
(f)
400 μm
Type-3 Cpx
(g)
Kfs+Ilm
Sieves
spongy core
500 μm
(h)
Kfs+Ilm
spongy mantle
200 μm
(I)
spongy mantle
Sieves
Kfs+Ilm
500 μm
(J)
Biotite glomerocryst
800 μm
(K)
Biotite
Cpx glomerocryst
800 μm
(L)
Biotite
Cpx glomerocryst
800 μm

DOI: https://doi.org/10.2138/am-2022-8744. http://www.minsocam.org/

Figure 3

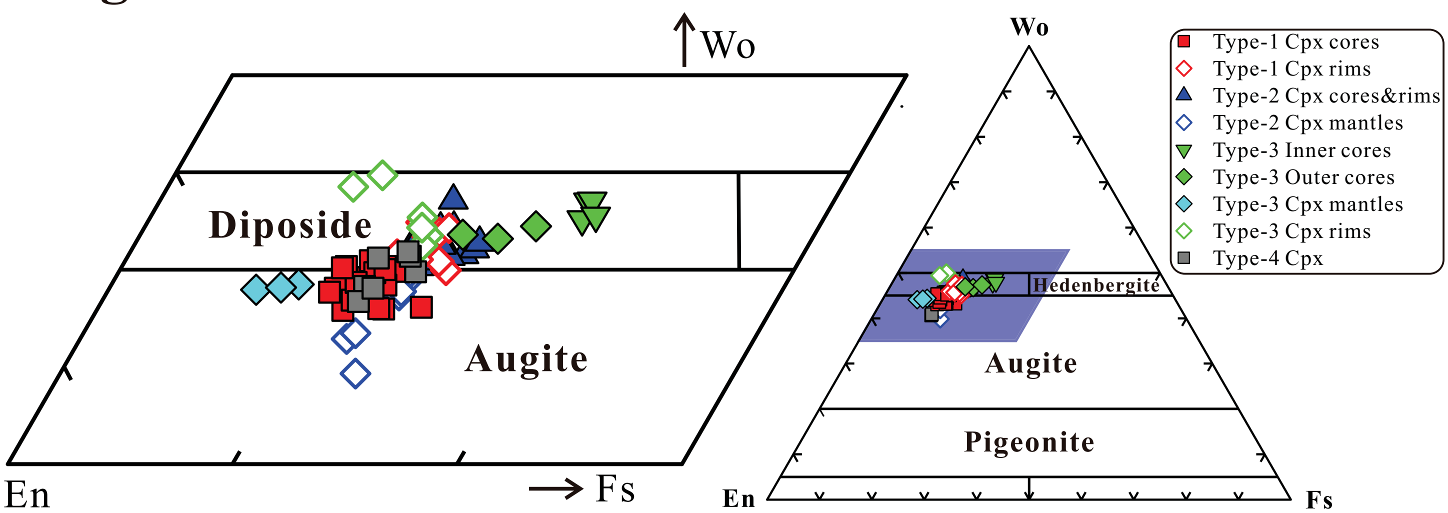

This is the peer-reviewed, final accepted version for American Mineralogist, published by the Mineralogical Society of America.
The published version is subject to change. Cite as Authors (Year) Title. American Mineralogist, in press.
DOI: https://doi.org/10.2138/am-2022-8744. http://www.minsocam.org/

Figure 4

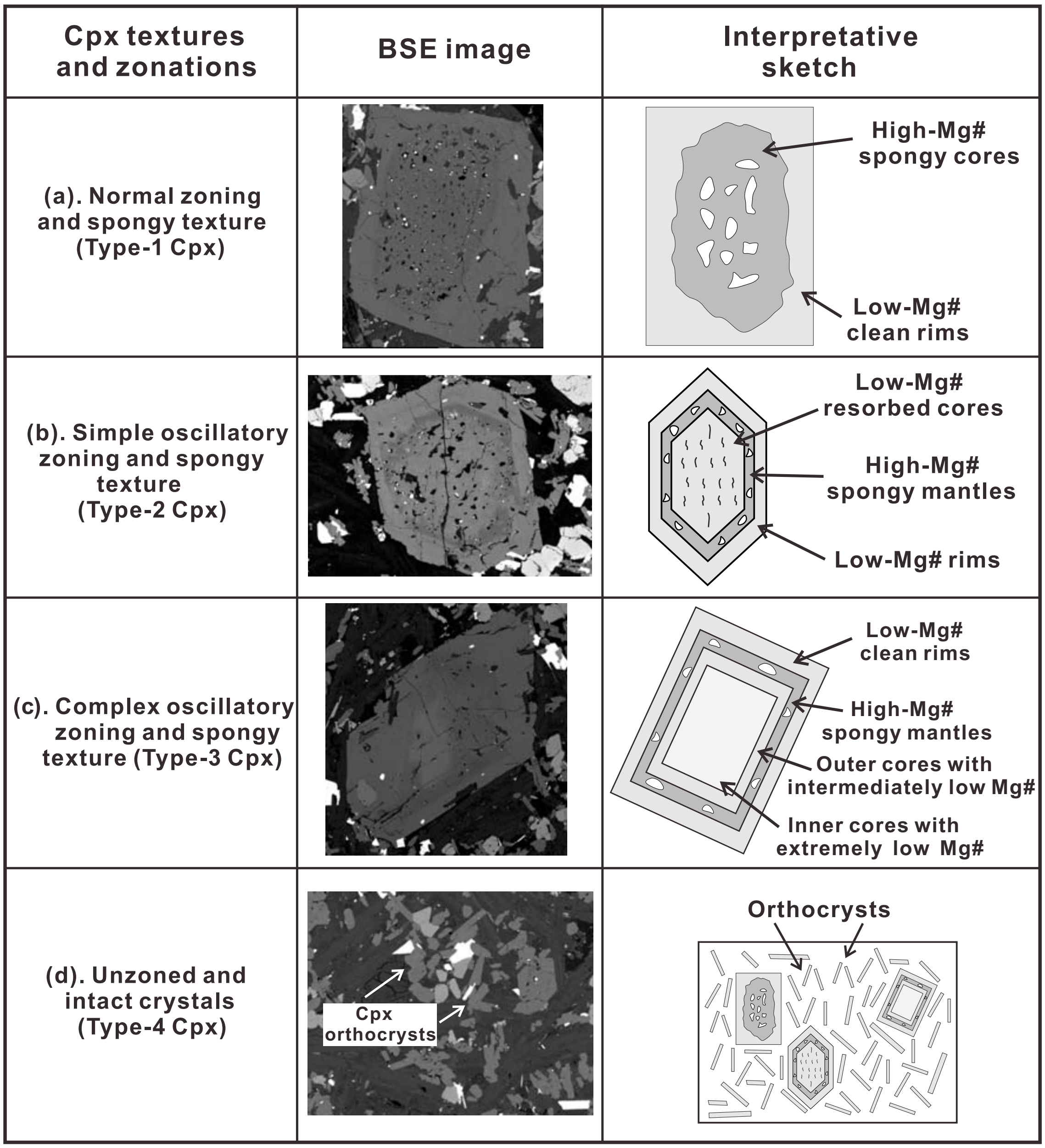

This is the peer-reviewed, final accepted version for American Mineralogist, published by the Mineralogical Society of America.
The published version is subject to change. Cite as Authors (Year) Title. American Mineralogist, in press.
DOI: https://doi.org/10.2138/am-2022-8744. http://www.minsocam.org/

Figure 5

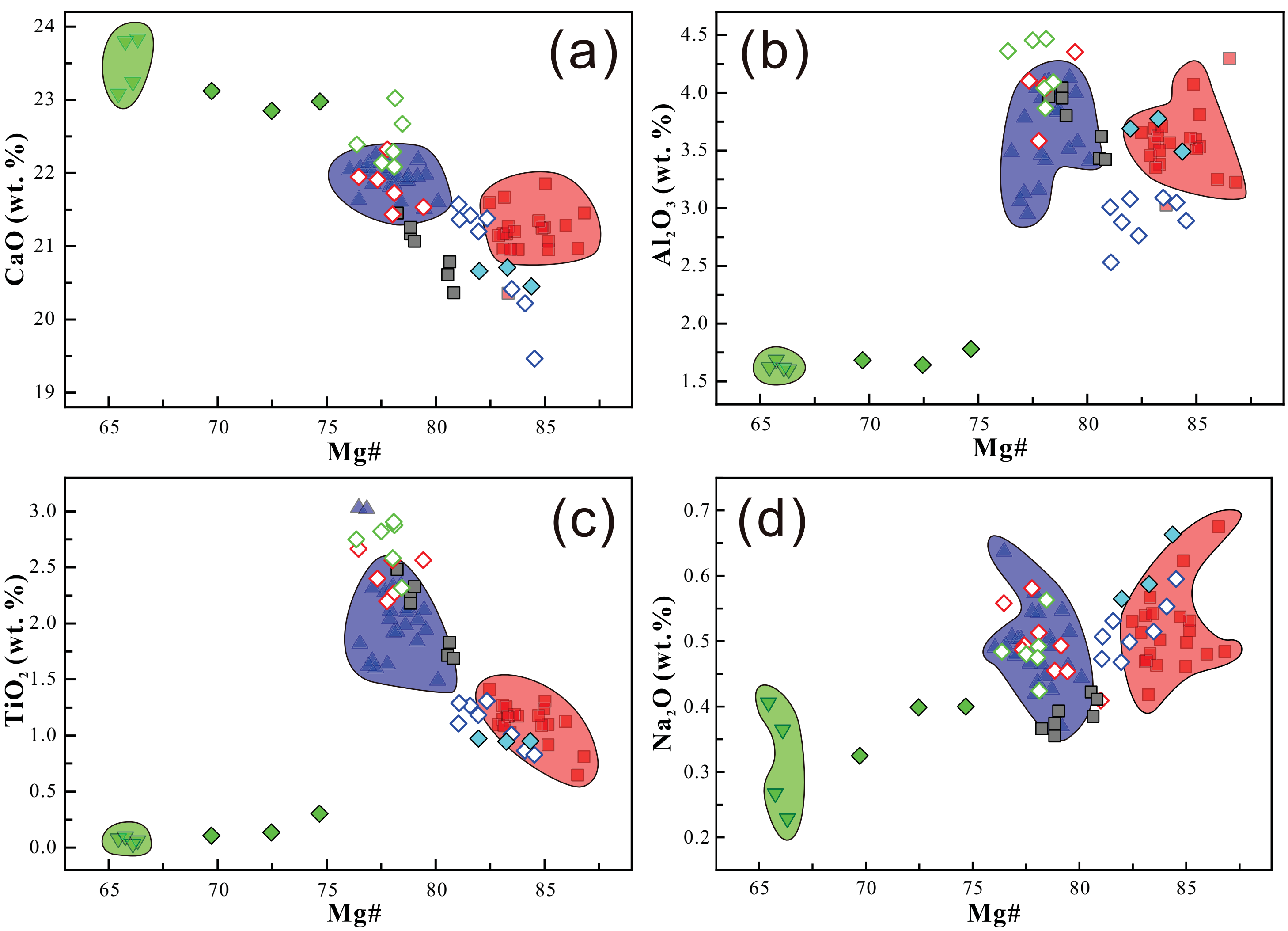

DOI: https://doi.org/10.2138/am-2022-8744. http://www.minsocam.org/

Figure 6

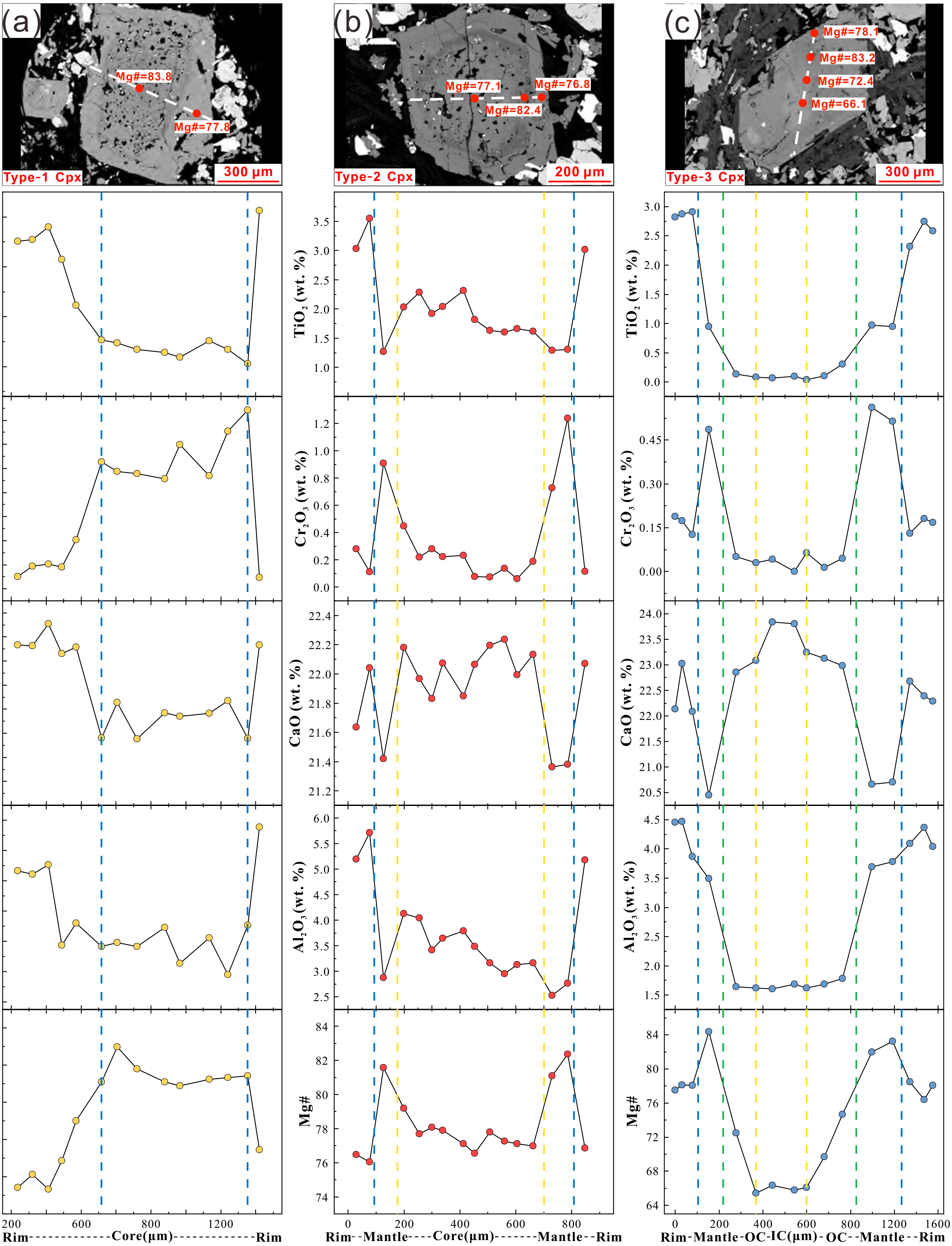

Figure 7

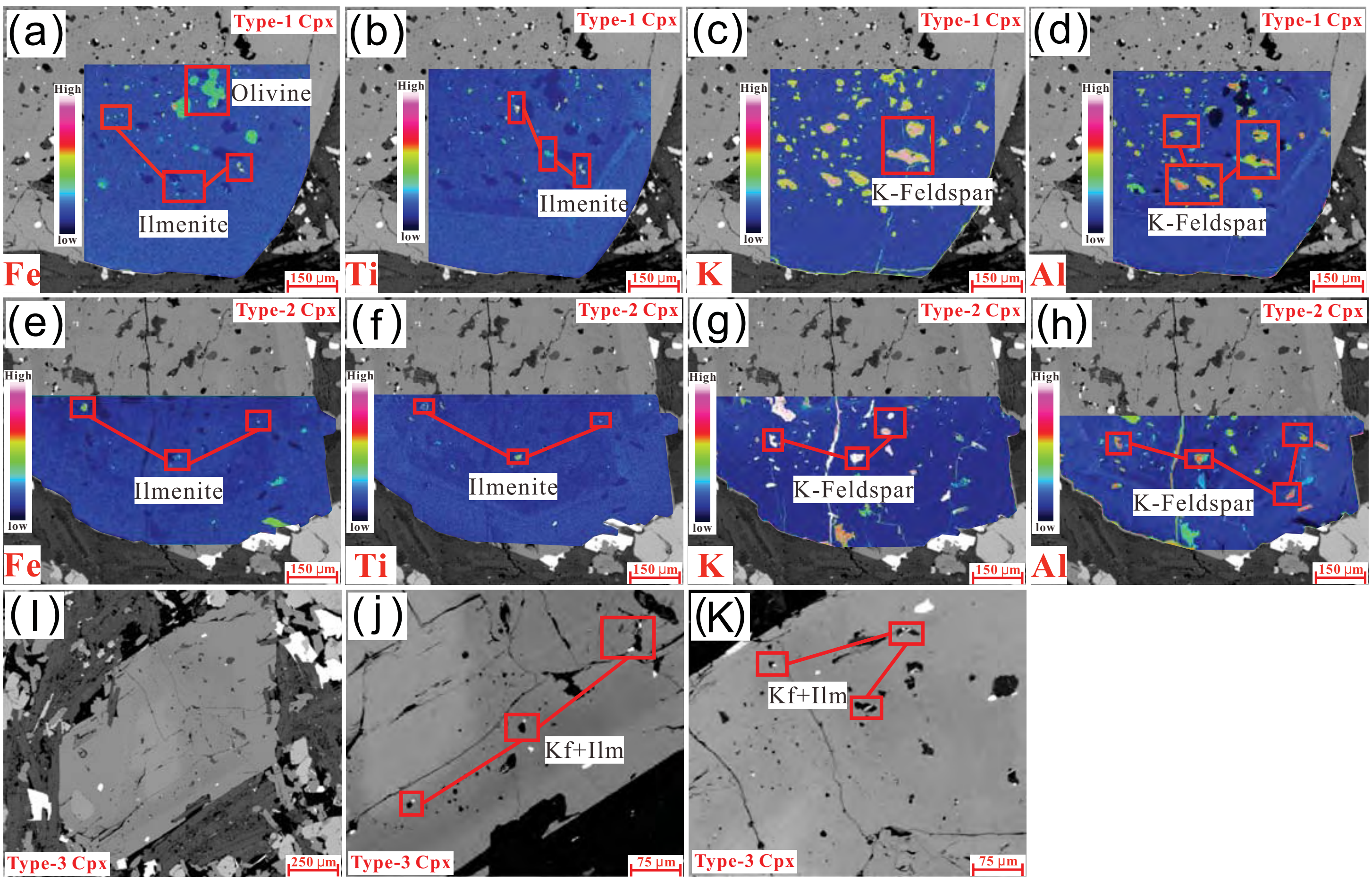
(a)
Type-1 Cpx
Olivine
Ilmenite
High
low
Fe
150 μm
(b)
Type-1 Cpx
Ilmenite
High
low
Ti
150 μm
(c)
Type-1 Cpx
K-Feldspar
High
low
K
150 μm
(d)
Type-1 Cpx
K-Feldspar
High
low
Al
150 μm
(e)
Type-2 Cpx
Ilmenite
High
low
Fe
150 μm
(f)
Type-2 Cpx
Ilmenite
High
low
Ti
150 μm
(g)
Type-2 Cpx
K-Feldspar
High
low
K
150 μm
(h)
Type-2 Cpx
K-Feldspar
High
low
Al
150 μm
(I)
Type-3 Cpx
250 μm
(j)
Kf+Ilm
Type-3 Cpx
75 μm
(K)
Kf+Ilm
Type-3 Cpx
75 μm

DOI: https://doi.org/10.2138/am-2022-8744. http://www.minsocam.org/

Figure 8

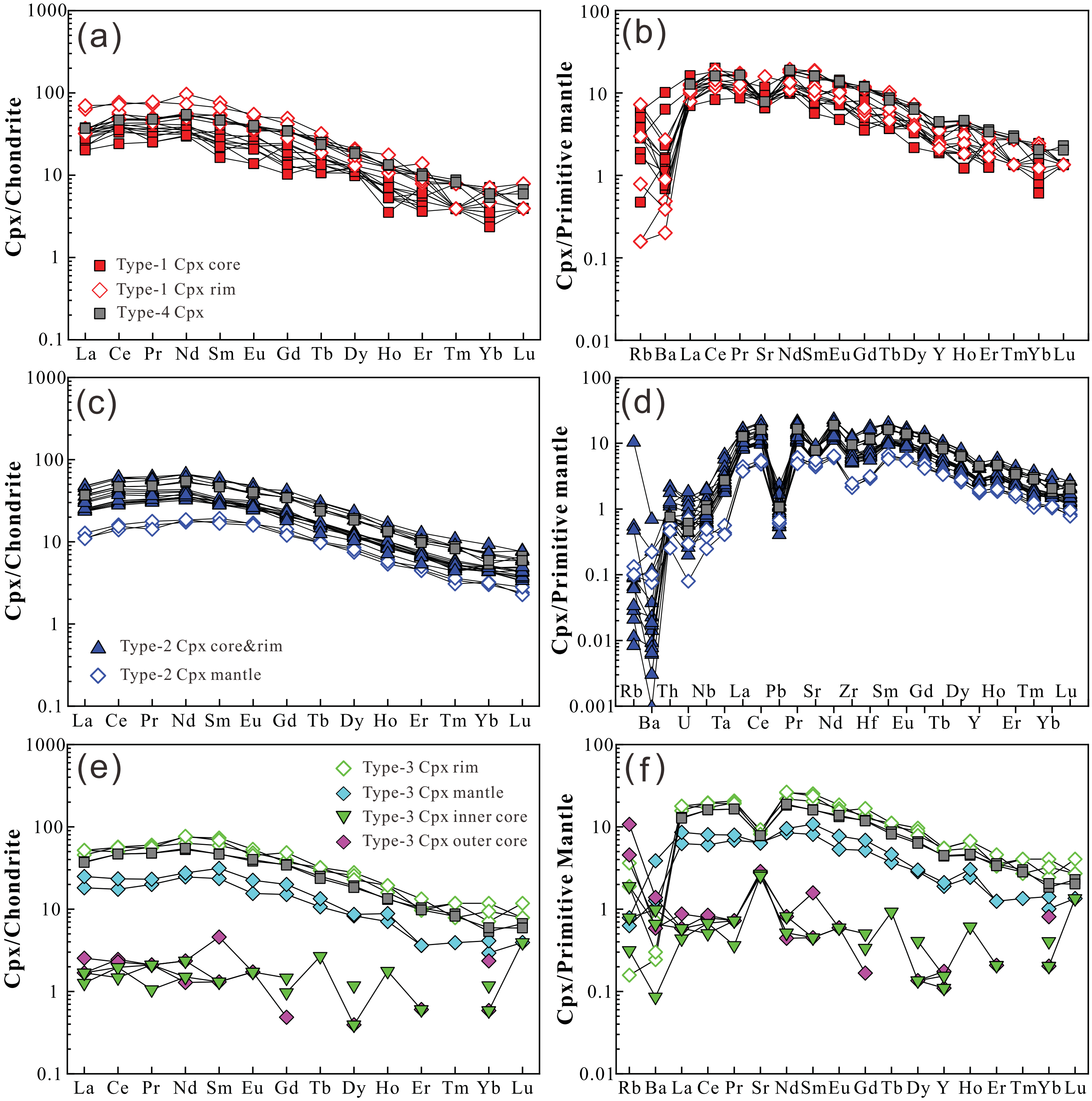

This is the peer-reviewed, final accepted version for American Mineralogist, published by the Mineralogical Society of America.
The published version is subject to change. Cite as Authors (Year) Title. American Mineralogist, in press.
DOI: https://doi.org/10.2138/am-2022-8744. http://www.minsocam.org/

Figure 9

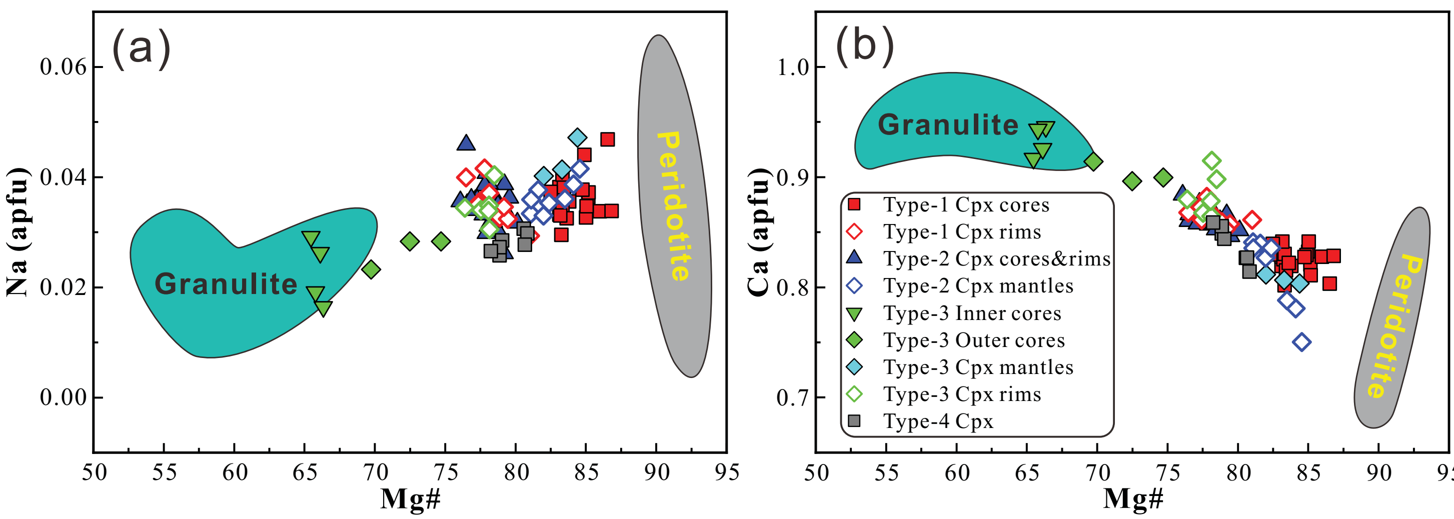

Figure 10

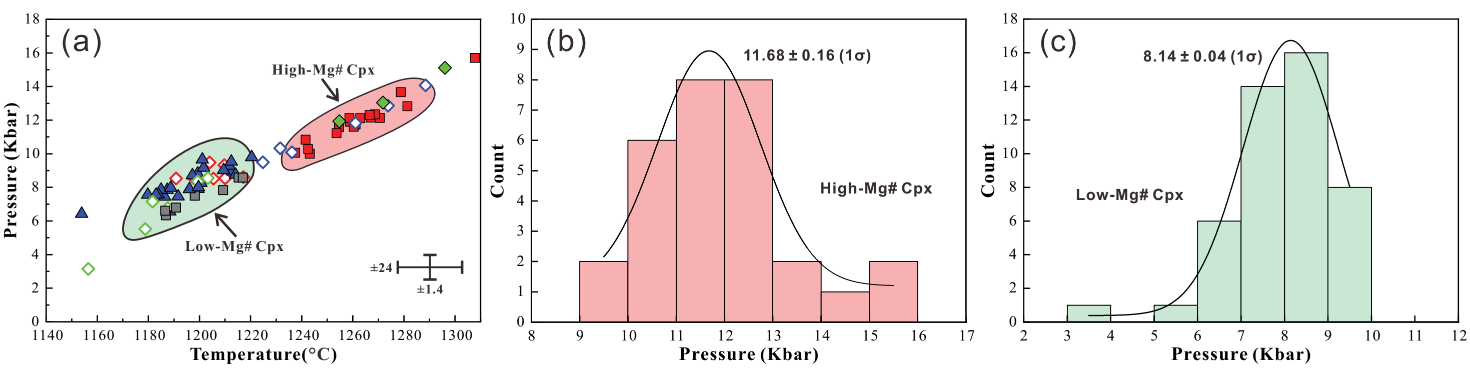
(a)
High-Mg# Cpx
Low-Mg# Cpx
±24
±1.4
Pressure (Kbar)
Temperature(°C)
(b)
11.68 ± 0.16 (1σ)
High-Mg# Cpx
Count
Pressure (Kbar)
(c)
8.14 ± 0.04 (1σ)
Low-Mg# Cpx
Count
Pressure (Kbar)

This is the peer-reviewed, final accepted version for American Mineralogist, published by the Mineralogical Society of America.
The published version is subject to change. Cite as Authors (Year) Title. American Mineralogist, in press.
DOI: https://doi.org/10.2138/am-2022-8744. http://www.minsocam.org/

Figure 11

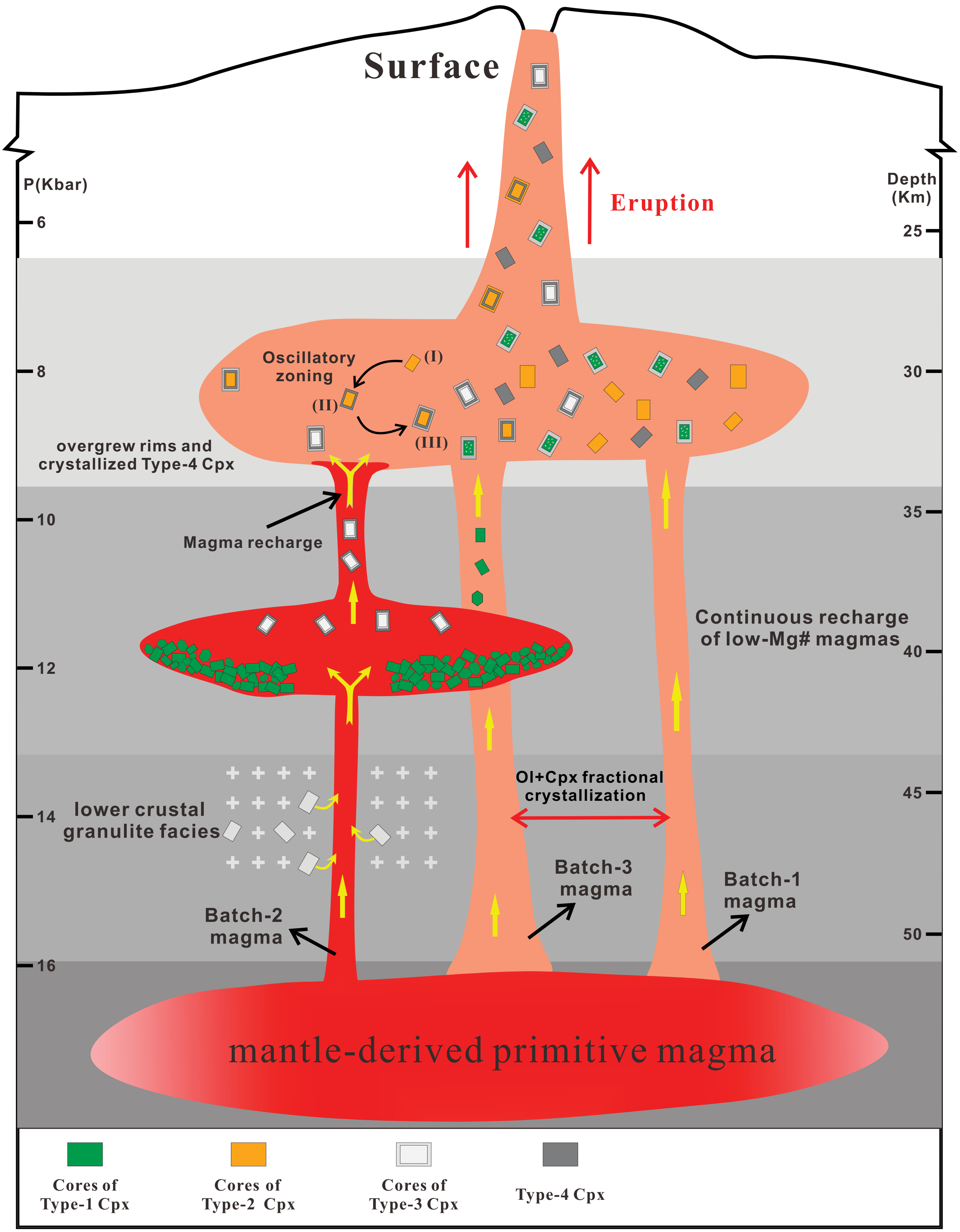

This is the peer-reviewed, final accepted version for American Mineralogist, published by the Mineralogical Society of America.
The published version is subject to change. Cite as Authors (Year) Title. American Mineralogist, in press.
DOI: https://doi.org/10.2138/am-2022-8744. http://www.minsocam.org/

Figure 12